Trough-scale Slope Countercurrent over the East China Sea Shelf Break Driven by Upwelling Divergence

Xuan Cui[1,2,3], , Dezhou Yang[1,2,3], Arthur J. Miller[4], Baoshu Yin[1,2,3], and Jiayan Yang[5]

[1] CAS Key Laboratory of Ocean Circulation and Waves, Institute of Oceanology, Chinese Academy of Sciences, Qingdao, China.

[2] College of Marine Sciences, University of Chinese Academy of Sciences, Beijing, China.

[3] CAS Engineering Laboratory for Marine Ranching, Institute of Oceanology, Chinese Academy of Sciences, Qingdao, 266071, China

[4] Scripps Institution of Oceanography, University of California, San Diego, La Jolla, California

[5] Department of Physical Oceanography, Woods Hole Oceanographic Institution, Woods Hole, Massachusetts, U.S.A

Corresponding author: Dezhou Yang (yangdezhou@qdio.ac.cn)

Baoshu Yin(bsyin@qdio.ac.cn)

Key Points:

- Over the entire East China Sea shelf break, the slope countercurrent beneath the surface Kuroshio Current is spatially continuous.
- The slope countercurrent is the western part of a deep cyclonic circulation in the Okinawa Trough.
- The upwelling divergence along the East China Sea continental slope is the main forcing mechanism of the slope countercurrent.

Abstract

Observations have revealed the existence of persistent slope countercurrents (SCCs) that flow southwestward beneath the Kuroshio Current at several locations over the East China Sea (ECS) continental slope. It was not clear whether these flows are localized circulation features or segments of a trough-scale circulation system in the Okinawa Trough (OT). We demonstrate that there indeed exists a continuous SCC along the ECS slope that is associated with an OT-wide cyclonic circulation using high-resolution model simulations and physical interpretations. The detailed features of the bottom OT circulation are illustrated by the trajectories of the Lagrangian drifters and the time-varying distributions of passive tracers. The SCC in the ECS is characterized by its weak yet persistent nature, typically located in narrow sloping regions at depths ranging from 500 to 1000 meters. It exhibits a characteristic speed of approximately O~(1) cm s^{-1}. Analyses and experiments suggest that the divergence of upwelling in the SCC layer (500-1000 m) gives rise to lateral potential vorticity flux, ultimately driving the deep oceanic OT circulation. Furthermore, the SCC also displays a substantial connection with the onshore intrusion of the Kuroshio Current, particularly to the northeast of Taiwan Island. The SCC may potentially play a crucial role in the transport of heat and nutrients, as well as in regulating sediment distributions within the deep OT. This mechanism offers fresh insights into explaining the presence of undercurrents beneath the western boundary currents in the global ocean.

Plain Language Summary

The Okinawa Trough (OT) is a key link between the Pacific Ocean and the East China Sea (ECS). It was observed by previous studies that persistent southwestward slope countercurrents (SCCs) exist beneath the northeastward Kuroshio Current at several locations over the ECS shelf break. These countercurrents have been attributed to a variety of mechanisms based on analyses and interpretations of observations made at different locations in the western OT. It is yet not clear whether these flows are localized circulation features or segments of an OT-wide circulation system. In this study, we find that there indeed exists a continuous SCC along the OT slope that is associated with an anti-clockwise circulation. Analyses indicate the OT experiences different vertical volume exchanges at the middle and bottom layer, which induces lateral exchanges of potential vorticity (a dynamically conserved quantity in an ideal and rotating fluid) and eventually drives the SCC. Numerical experiments are performed to show the validity of this process. The SCC may be of vital importance in transporting heat and nutrients, and regulating the sediment distributions in the OT. This mechanism is potentially applicable to explain the undercurrent beneath the western boundary currents in the global ocean.

1 Introduction

The global ocean circulation system is spatially complex and temporally evolving. Many of its aspects remain insufficiently understood, especially in the deep ocean beneath the main thermocline where direct observations are still sparse. Stommel (1958) and Stommel and Arons (1960) constructed the first conceptual model of abyssal circulation in their attempt to explain how the North Atlantic Deep Water is exported away from its formation sites in the subpolar North Atlantic Ocean. It is postulated that deep western boundary currents must play a critical role in transporting water masses meridionally, which has been confirmed by subsequent observations (e.g., Warren and Speer, 1991; Toole et al., 2017) in the Atlantic Ocean and elsewhere (e.g., Andres et al., 2015; Beal and Bryden, 1997).

The abyssal ocean circulation in the North Pacific Ocean is distinctly different from that in the North Atlantic Ocean because of a lack of deep-water formation. Observations, however, have revealed the existence of southwestward countercurrents (SCCs) beneath the Kuroshio Current over the ECS shelf break, which also serves as the western boundary of the Okinawa Trough (OT). Lie et al. (1998) were the first to identify and actually named this current. Their analyses of mooring observations revealed a quasi-permanent SCC in the northern OT and a wave-like SCC feature in the central OT. They attributed the SCC formation mechanism in the northern and central OT to the upwelling associated with KC branching and frontal eddies. The SCC is also observed in an inverted echo sounder array by James et al (1999) where the velocity maximum is located at 800-m depth. Nakamura et al (2003, 2008) concluded that the SCC is relatively stronger and deeper in the southern basin of northern OT than in the northern basin and its variability is highly influenced by the Kuroshio path meander. As for the SCC mechanism in the northern OT, Nakamura et al. suggested that, based on analyses of numerical model simulations, deep cyclonic eddies are the main cause of the observed countercurrent. Based on a 23-month acoustic Doppler current profiler observation, Andres et al. (2007) also showed the existence of the SCC at the P-N line in the ECS. Due to the lacking of simultaneous observations in the OT and the limited understanding of the deep ocean circulation, southwestward flows beneath the Kuroshio Current at different observing sites have been considered as parts of localized circulations that are attributable to local processes (Nakamura et al., 2008). More systematic analyses of the OT-wide dynamical processes are needed so that a better understanding of SCC mechanisms, either local or basin-wide, can be developed.

In semi-enclosed deep basins, the sense boundary flows are strongly constrained by the lateral fluxes of the potential vorticity (PV) (Yang and Price, 2002; 2007). A positive PV flux would require a cyclonic boundary current so that the frictional PV flux balances the lateral advective PV flux. This PV integral constraint has been applied to explain boundary circulations in several marginal seas, such as in the Arctic Ocean (Yang, 2005; Karcher et al., 2007), and the South China Sea (Lan et al., 2013; Zhu et al., 2017; Gan et al., 2019). The OT is a semi-enclosed basin with several breaches for the deepwater layer and the SCC can be considered as the western boundary current of the deep circulation within the OT. In this study, we will investigate whether the existence of the SCC is influenced by the lateral PV advection into this semi-enclosed basin.

The remainder of the paper is structured as follows. Section 2 offers a brief introduction to the numerical model, encompassing its configuration, validation, and the inclusion of drifters and tracers. In Section 3, a comprehensive discussion of the circulation features is presented through analyses of our model results. The formation mechanism of the SCC is outlined and validated in

Section 4. The discussion part section 5 incorporates relevant features and experiments. Finally, Section 6 provides concluding remarks.

2 Numerical model

2.1 **Model setup**

The numerical model in this study is based on the Regional Ocean Model System (ROMS), a free-surface, terrain-following, primitive equation ocean model (Dinniman et al., 2003; Marchesiello et al., 2003; Peliz et al., 2003; Shchepetkin & McWilliams, 2005). ROMS has been widely used in various oceanographic studies. Detailed information about the model can be found in the works of Shchepetkin and McWilliams (2003, 2005).

In this study, we use the ECS-SCS ocean model (ESOM) from Yang et al. (2018) to simulate climatological ocean circulation in the OT (see Figure 1 for the model domain). Extending from 105°E to 136°E and from 15°N to 41°N, ESOM has a horizontal resolution of 3′×3′(~5 km) and 31 vertical layers. Shown in Figure 1, the OT is a deep and narrow It is worth noting that the maximum grid stiffness ratios, rx0=1.62 (Haney, 1991) and rx1=3.72 (Beckman and Haidvogel, 1993), which suggests ESOM grids is fine enough to reflect the steep slope topography without causing instability problems or spurious deep currents. In addition, ERA-Interim reanalysis wind stress with a time span of 12 h (Dee et al., 2011) is used to force the Nest2 model, river fluxes of the Yangtze River and the Pearl River (http://xxfb.hydroinfo.gov.cn) and 10 tidal components from the TPXO7 (Egbert and Erofeeva, 2002) are included in ESOM. Atmosphere forcings are utilized from COADS data. (Diaz et al., 2002) Feeds by the open boundary conditions from a larger grid domain (fully spun up to cover the Anderson and Gill timescale) including the whole Pacific Ocean, ESOM has been consistently integrated for 15 years for the spin-up process. The 15th-year output from the spun-up ESOM the is utilized to analyze the circulation features over the ECS slope. All the configuration details can be accessed in Yang et al., 2018.

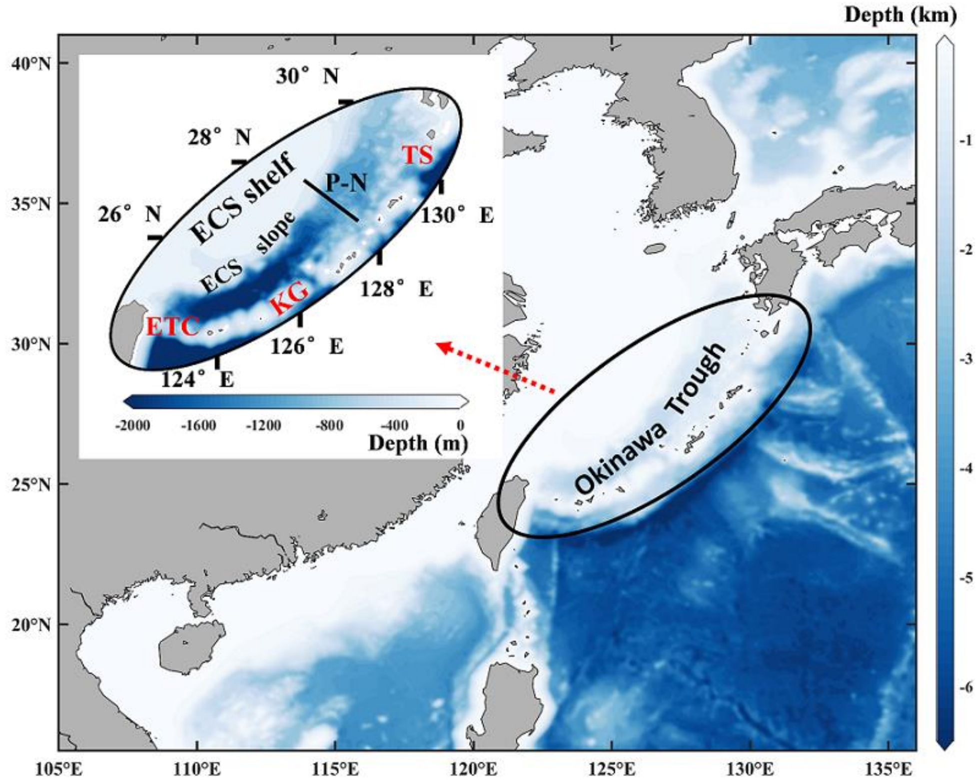

Figure 1. Geographical setting and model domain. The black ellipse delineates the research domain, encompassing the East China Sea slope and the Okinawa Trough (OT). The P-N transect is marked with the black solid line. The deep channel linking the Okinawa Trough and the Pacific Ocean is highlighted with red characters: ETC, east Taiwan channel; KG, Kerama Gap; TS, Tokara Strait.

2.2 **Model validation**

ESOM has undergone rigorous validation, consistently demonstrating strong agreement with the observations available in previous studies on ocean circulations in the ECS regions (Yang et al., 2018; Yang et al., 2020), such as the Kuroshio Current, the Taiwan Warm Current, and the Tsushima Warm Current. ESOM also performs well in regions with steep and complex topography where Kuroshio onshore intrusions often take place (Cui et al., 2021).

Although the ESOM output was intensively checked in previous studies, we execute an extra model validation by comparing the velocity structure at the well-studied P-N line with accessible observations from Andres et al., 2008. Figure 2a shows the velocity across the section along the well-studied P-N line in the control run. In the upper layer, the most significant feature is the northeastward Kuroshio Current. The Kuroshio Counter Current (KCC), which flows southwestward, can be observed at the right side of the Kuroshio Current. The horizontal velocity structure aligns with the velocity profile across a Munk frictional boundary layer, as described by Pedlosky (1979) and Qiu & Imasato (1990). Significantly, it distinctly illustrates the presence of the SCC beneath the core of the Kuroshio Current, the typical velocity of which is about O~(1) $cm \cdot s^{-1}$. Overall, the modeled velocity structure across the P-N line compares well with observational pattern in Figure 2b. Therefore, we are confident that ESOM is an appropriate tool for the purpose of this study.

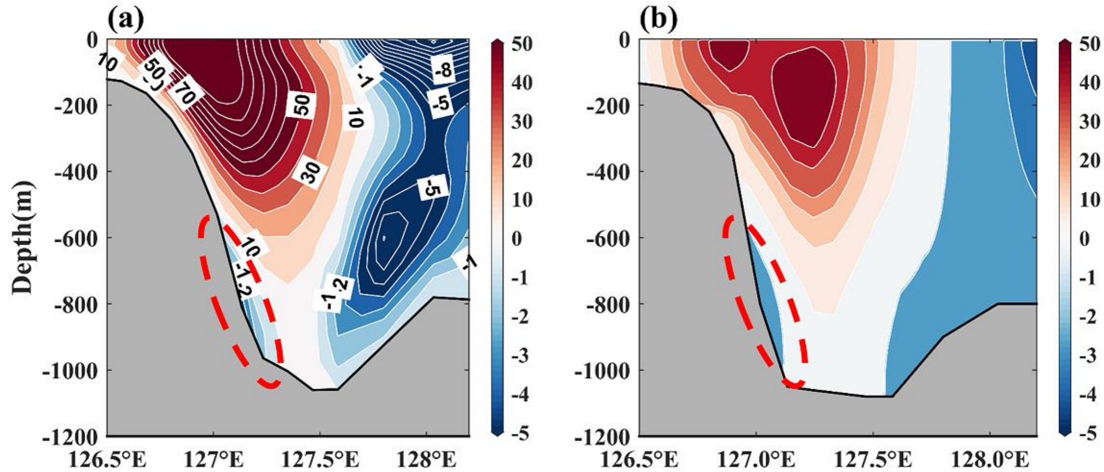

Figure 2. Annual mean cross-transect velocity at P-N line from the model **(a)** and output **(b)** observations (reconstructed from Andres et al., 2008). The red ellipse marks the slope countercurrent. Northeastward positive, unit: cm s^{-1}.

2.3 Lagrangian drifters and passive tracers

To comprehend the characteristics of the modeled deep circulation, three-dimensional Lagrangian drifters are deployed at every rho point of the ESOM grid within the OT, where the bathymetry ranges from 500 to 1000 meters. Unlike isobaric and geopotential drifters, these Lagrangian drifters are designed to accurately capture the genuine movement of water particles, with their three-dimensional positions computed at each time step. As illustrated in Figure 3a, these drifters are positioned 20 meters above the ocean bottom within the OT which ensures that they remain outside the bottom boundary layer and are partially captured by the SCC core. Released at the first day of January, these drifters are tracked for 360 days and are recorded every 36 hours to filter the tidal signals.

Passive tracers (which do not contribute to the equations of motion) are also released within the OT to gauge the mass transport of deep currents. There are generally two ways to introduce tracers into numerical simulations. One approach involves specifying a tracer distribution at the initial state, integrating it over time, and observing the resulting concentration as it plays out; the alternative method, which is applied in this study, involves continuously dying specific parts of the water column with tracers at a particular concentration, effectively designating these locations as point sources for tracers. Apart from temperature and salinity, we additionally introduce two groups of passive tracers into the model computation. Tracer 1 is concentrated in the northern part of the OT at a depth ranging from 500 to 1000 meters (see Figure 3b), while tracer 2 is uniformly distributed throughout the OT at the same depth range. This technique has been utilized by a group of studies (Hu et al., 2020; Yang et al., 2018; Isobe et al., 2006).

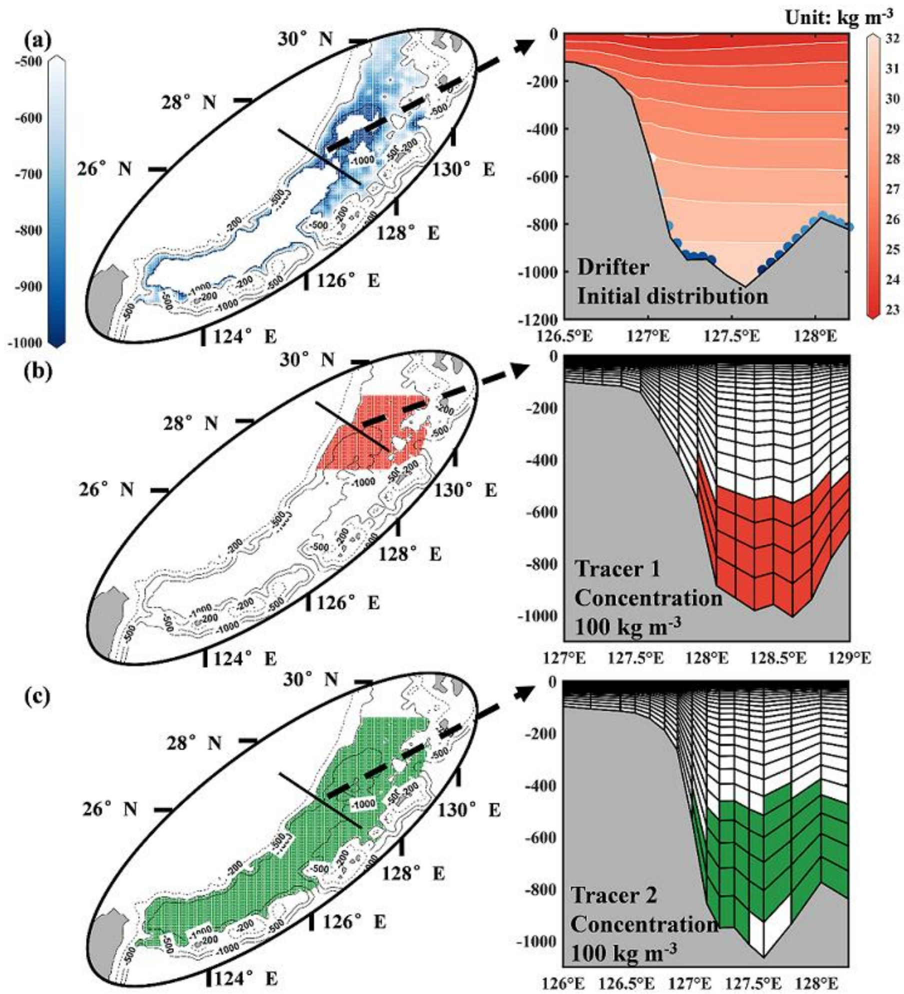

Figure 3. Initial distributions of 3-dimentional Lagrangian drifters and point sources of passive tracers. **(a)** Initial locations of drifters on the left panel with color representing their depths, and on the right panel the drifter distribution at the P-N line, overlapping the density anomaly (background density=1000 kg m^{-3}). **(b)** Horizontal distribution of point-source tracer 1 at the left panel, and on the right panel the vertical structure at the marked transect in the ellipse. **(c)** Horizontal distribution of point-source tracer 2 at the left panel, and vertical structure at the P-N line on the right panel.

3 Circulation features in the deep OT

Earlier studies have illustrated the bottom intensified feature of SCC (Nakamura et al., 2005, 2008; Andres et al., 2008). To distinctly depict this characteristic (where the velocity maximum occurs at the bottom), we present the circulation at the bottom terrain-following layer across the OT, with the 500-meter isobaths overlaid in Figure 4a. The SCC, characterized by a maximum speed exceeding 6 cm s^{-1}, exhibits continuity along the deep western boundary. On the eastern side of the OT, a relatively weaker current flows northeastward along the western side of the Ryukyu Islands. This northeastward current tends to intensify northeast of Taiwan but weakens as it passes the Okinawa and Amami Islands. Collaboratively, these two currents give rise to a cyclonic circulation beneath the 500-meter depth threshold in the OT. The main axis of this cyclonic circulation is positioned around 700 to 800 meters (refer to Figure 2a). Importantly, a well-defined cyclonic eddy is located in the northern OT region, near S1, contributing to a localized intensification of the Subsurface Countercurrent (SCC). Along the western boundary of the Tokara Islands, the Kuroshio Counter Current (KCC) coincides with the cyclonic circulation, exhibiting a distinct southward flow at coordinates 129°E, 29.5°N.

The presence of SCC along the ECS slope is furtherly illustrated by three extra cross-shelf transects. We choose three representative transects over the entire ECS slope to show the previously observed SCCs are not localized circulation features but rather a spatially continuous circulation over the ECS shelf break. It is worth mentioning that EOSM offers up to 3 vertical layers at the SCC region (see Figure 4b), which provides a fine enough resolution to resolve the SCC as well as its bottom-intensified feature. Figures 4c to 4e depict the normal velocity across transects S1 to S3. The circulation within the sloping area is characterized by a southwestward current, flowing counter to the direction of the surface Kuroshio Current. Although the SCC exhibits spatial variations in terms of depth range, width, and velocity maximum, it is predominantly confined to the depth range of 500 to 1000 meters throughout the ECS slope.

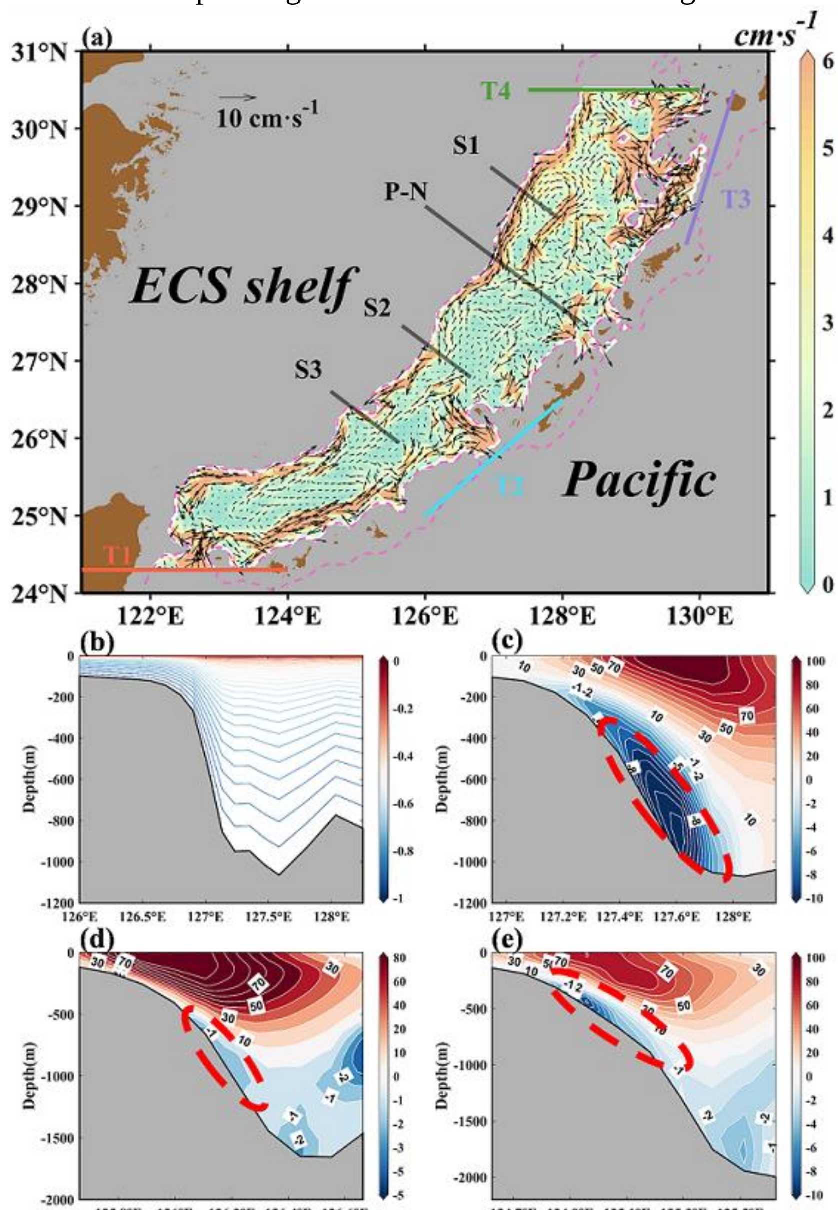

Figure 4. Deep circulation in the Okinawa Trough. **(a)** Annual mean bottom currents. The pink dashed lines are the 500-m isobaths. Regions shallower than 500 m or out of the Okinawa Trough are masked by gray shading. T1~T4 serve as four pathways enabling the exchange of deep water. The P-N line, and S1~S3 are cross-shelf transects at the ECS shelf break. **(b)** Terrain-following S coordinate at P-N line, with -1 indicates the ocean bottom, and 0 corresponds to the sea surface. **(c)~(e)** show the normal velocity at S1~S3, respectively (northeastward positive). The SCC is highlighted by the red dashed ellipses.

Although the deep circulation is extremely complex with numerous details, the trajectories of groups of drifters share some similarities, and the envelope of the SCC is intricately sculptured by the trajectories of the Lagrangian drifters. Three groups of drifters are summarized, with their trajectories represented by colored asterisks in Figure 5. Additionally, their time-varying depths are plotted in red, green, and yellow, respectively. Group 1 is centered at the northern part of the ECS slope, and the trajectories of which indicate that these drifters are advected southward, adhering closely to the ECS slope. After a 1-year travelling time, these drifters are capable of reaching the steep topography northeast of the Taiwan Island. Drifters in group 2 are initially deployed at the heart of the OT where the bathymetry is shallower than southern part. After releasing, drifters in group 2 are firstly carried northward to shallower region, and then meet with the southwestward SCC. The subsequent trajectories highly resemble those in group 1. It is also interesting that the trajectories released at the central ECS slope in group 3 alter their directions and travel northeastward along the eastern boundary of the OT, which implies the circulation in the deep OT may potentially be connected.

The temporal development of tracer 1 concentration confirms the southwestward SCC from another perspective. Shown in Figure 6, tracer 1 is generally diffused southward after initialization. However, a sharp front emerges at the western edge of the OT due to the southwestward transport facilitated by the SCC. Approximately 350 days later, another sharp front develops at the eastern boundary, possibly associated with the northeastward advection of the robust Kuroshio Current on the right side of the SCC.

These findings substantiate our perspective that the SCC represents a spatially continuous flow linked to the trough-scale cyclonic circulation. In the subsequent sections, we define the SCC layer in ESOM simulations as the depth range of 500 to 1000 meters for further analyses.

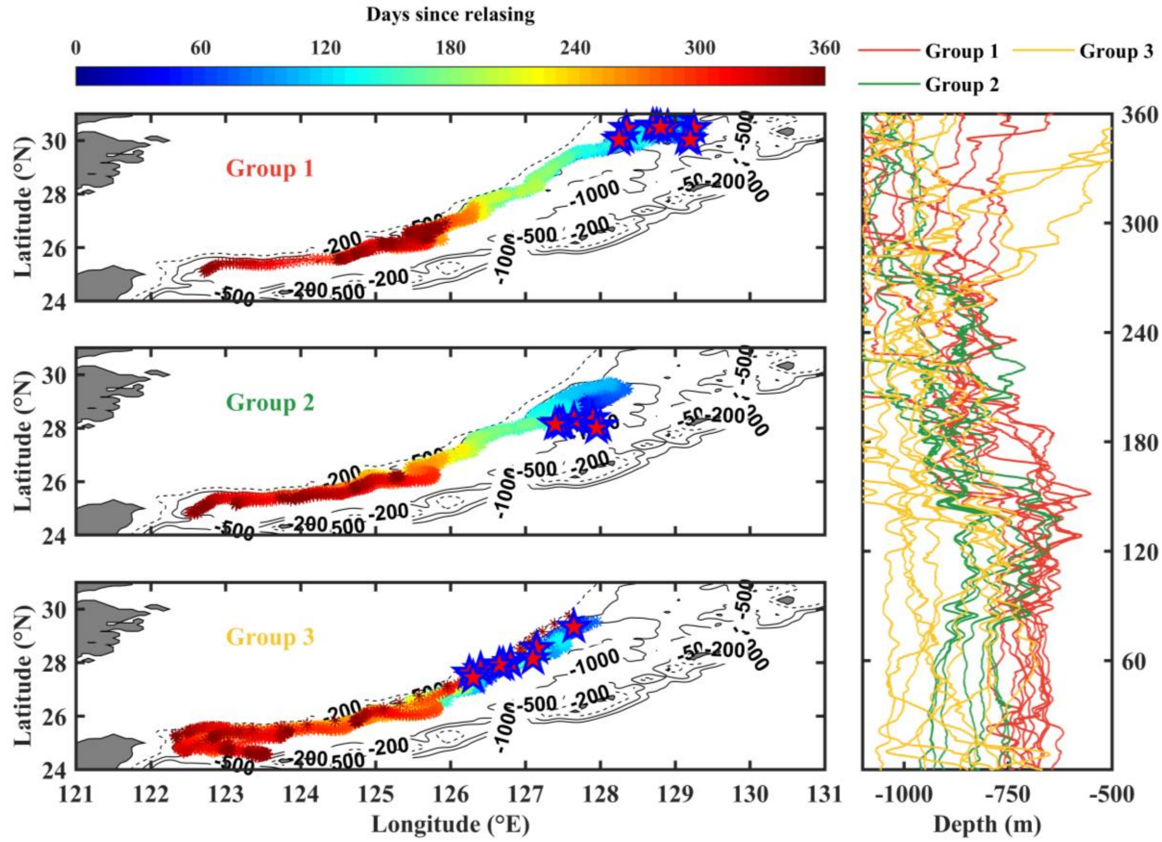

Figure 5. Trajectories of different groups of Lagrangian drifters which are selected to represent the downstream pathway of the slope countercurrent. The left three panels respectively depict the drifters released at the northern ECS slope, the heart of the Okinawa Trough, and the central ECS slope. The right panel are the time-evolving depths of the different groups of drifters. These drifters are recorded every 36 hours.

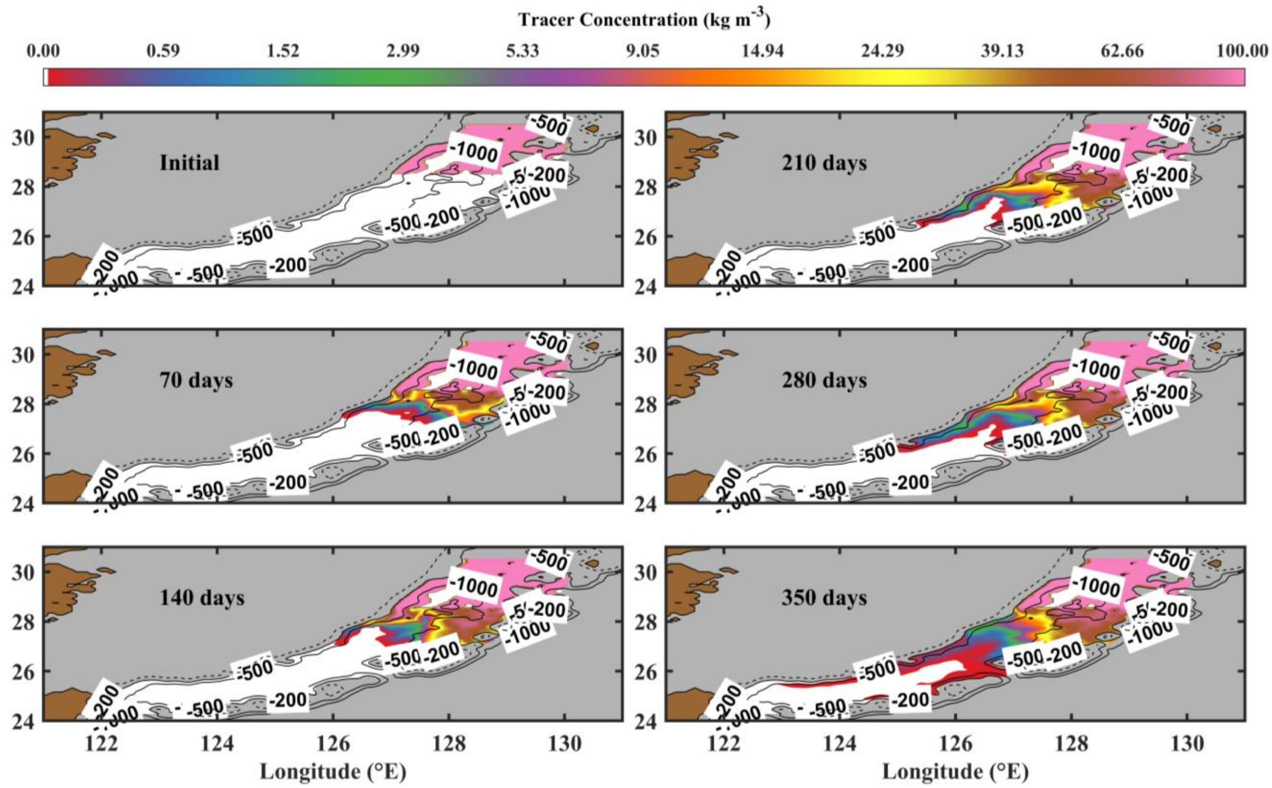

Figure 6. Time-varying tracer concertation at the bottom terrain-following layer for tracer 1. The dashed line represents the 200-meter isobaths, while the 500-meter and 1000-meter isobaths are indicated by solid lines. Regions shallower than 500 meters or beyond the Okinawa Trough are masked with gray shading.

4 Mechanism

4.1 **Potential vorticity budget**

In the case of a semi-enclosed deep basin like the OT, the deep circulation is typically linked to lateral exchanges of volume flux (LV flux). The OT undergoes substantial exchanges of deep water with adjacent seas, primarily through four breaches, as illustrated in Figure 4a for their locations. Transect 1 (T1) is situated at the East Taiwan Channel (ETC), where the lower envelope of the Kuroshio Current extends to 1 km. Transect 2 (T2) is located at the Kerama Gap, dominated by inflow from the northwest Pacific Ocean. Transect 3 (T3) is positioned at the Tokara Strait, representing the exit point of the Kuroshio Current from the OT. Transect 4 (T4) is positioned at the northern edge of the OT, where part of the lower-layer water may penetrate onto the shelf, serving as one of the sources of the Tsushima Current.

Figure 7a illustrates the deep lateral volume fluxes (500~1000 m) through these transects (inflow considered positive) in the control run. The transport into the OT predominantly occurs across T1 and T2, with annual mean values of approximately 1.35 Sv and 0.48 Sv, respectively. The primary outflow transport from the OT takes place through T3, accounting for approximately 1.63 Sv annually. The volume flux across T4 is minimal at 0.01 Sv, rendering it negligible in comparison to the fluxes across T1 to T3.

The LV fluxes through T1 to T4 advect potential vorticity (PV) and directly influence the PV budget in the Open Topology (OT). To elucidate the mechanism behind the cyclonic circulation in the lower layer of the OT, we employ the PV constraint (Yang and Price, 2000, 2007; Yang, 2005) :

$$\sum_{i=1}^{N} \frac{Q_i f_i}{H_i} = -\lambda \oint_C (\boldsymbol{u_h} \cdot \boldsymbol{l})\, ds + Res \qquad (1)$$

In equation (1), C is a closed circle, $\boldsymbol{l}$ is the unit vector tangential to C, ds is an element length. The term $\sum_{i=1}^{N} \frac{Q_i f_i}{H_i}$ is the net PV flux across C (influx positive), where Q_i, f_i, and H_i are respectively the volume transport, Coriolis parameter, and the thickness at the *i*th breach. The term $-\lambda \oint_C (\boldsymbol{u_h} \cdot \boldsymbol{l})\, ds$ is the lateral (bottom) frictional torque (LF torque hereafter), where λ is the Rayleigh friction coefficient, $\boldsymbol{u_h}$ is the horizontal component of the velocity vector. The term *Res* denotes the residual including the accelerating term and is usually omitted at an annual-mean state. Equation (1) is in a simplified form but can be applicable below the thermocline (Zhu et al., 2019, 2017), the depth of which is 300 m at most over the ECS slope. It states that the net lateral PV flux into an area bounded by a closed contour C is balanced by the lateral frictional torque. A positive net PV flux, for instance, is balanced by an anti-cyclonic frictional torque, which is often associated with cyclonic circulation along C.

Yang and Price (2000, 2007) conducted a series of idealized numerical experiments using a reduced-gravity model to investigate the influence of the PV constraint on boundary currents. In this study, we employ ESOM simulations to investigate whether the deep cyclonic circulation in the OT, especially the SCC, is linked to lateral PV fluxes.

The horizontal velocity at the depth of 800 meters, where the core of the SCC is situated, signifies the velocity within the SCC layer The lateral frictional torque (LF torque) is integrated along the closed circle outlined in Figure 7b, approximately following the 800-meter isobath. The Rayleigh friction coefficient λ is typically assigned subjectively. For example, Yang and Price (2000) utilized $\lambda = 1.36 \times 10^{-6}\ s^{-1}$. Huang and Yang (1996) directly estimated $\lambda \sim 10^{-6}\ s^{-1}$. Here we apply a rigorous approach to set λ by applying linear regression to these variables The linear regression coefficient yields $\lambda = 5.17 \times 10^{-6}\ s^{-1}$in Figure 7c). The temporal evolution of the net PV flux and the LF torque is shown in Figure 7d, it is estimated an annual net PV influx of 0.082 m^2s^{-2}enters the deep OT. The corresponding LF torque is 0.057 m^2s^{-2}, indicating nearly 70% of the total PV flux is dissipated through bottom friction. It is noteworthy that the lateral frictional torque (LF torque) is positively correlated with the net potential vorticity (PV) flux at a 1-month lag, with a correlation coefficient exceeding 0.65 at the 95% significance level. This suggests that the LF torque adjusts to the PV flux on a 1-month timescale, indicating that the PV flux serves as the reason for the deep cyclonic circulation and, consequently, the SCC.

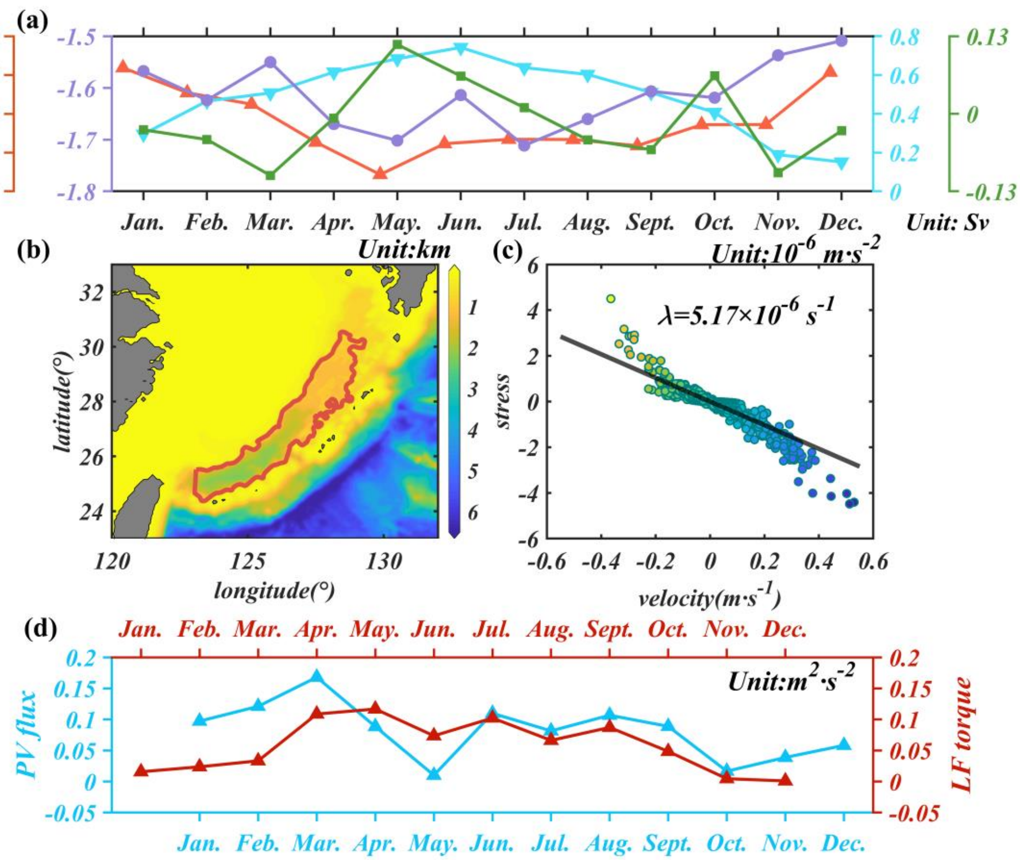

Figure 7. Volume and PV fluxes into (out of) the Okinawa Trough. **(a)** The monthly mean volume flux (500-1000 m) across the transects T1-T4 (red for T1, cyan for T2, purple for T3, and green for T4). **(b)** Integration circle for frictional torque computation which roughly matches the 800-m isobaths in the Okinawa Trough. **(c)** The linear regression of the bottom stress as a function of bottom velocity (northward or eastward positive). **(d)** The monthly mean net PV flux entering the Okinawa Trough versus the lateral frictional torque term. PV, potential vorticity.

Designing numerical experiments to verify the PV constraint with primitive-equation models (like ROMS) is challenging, especially in an irregular shaped basin like the OT. It is tempting but impractical to freely manipulate the lateral PV input into the OT and observe the corresponding response in the deep circulation. Modifying fluxes at the model boundary is a straightforward task, but it typically has minimal impact on the interior of the model. On the other hand, it is even less feasible to directly alter the fluxes at T1~T4. However, this dilemma is resolved by leveraging the unique characteristics of the western boundary regions through the following approach.

Circulations over 2000-m depth in the western boundary regions are significantly influenced by large-scale forcings, such as the wind stress curl and its associated signals. These factors are encompassed in the open boundary conditions of regional models like ESOM. In essence, western boundary regions serve as the recipients of open boundary messages, and changes in the open boundary conditions will definitely affects circulation feature in the OT. The deep cyclonic circulation (indicated by the red line in Figure 7d) exhibits significant seasonal contrast between July and January, a pattern consistent with the ECS Kuroshio intensity as reported by previous studies (Hu et al., 2020; Yang et al., 2018; Guo et al., 2006, 2003).

Therefore, the disparity in open boundary conditions between January and July may partly contribute to the variation in the deep circulation. To validate this deduction, we conducted three additional cases by modifying the open boundary conditions (see Figure 1 for boundary locations). Case BRY07 and case BRY01 are run under fixed open boundary conditions in July and January from the coarse model in all 12 months to simulate scenarios with different net PV fluxes into the OT (see Table 1 for details). Since the seasonal fluctuations from the open boundary conditions are eliminated in BRY07 and BRY01, a BRYAN case is performed with fixed open boundary conditions at an annual climatology state as a reference.

Table 1

Numerical Experiments in this Study

<table>
<tr><th>Case name</th><th>Modification</th><th>Integration period</th><th>Description</th></tr>
<tr><td>Control</td><td>--</td><td rowspan="11">14th to 15th model year, the 15th-year output for analyze</td><td>Climatological simulation</td></tr>
<tr><td>BRY07</td><td rowspan="2">Open boundary conditions fixed at July (January) 15th</td><td rowspan="2">Alter PV influx through changes in basin-scale signals included in open boundary conditions</td></tr>
<tr><td>BRY01</td></tr>
<tr><td>BRYAN</td><td>Open boundary conditions fixed at annually climatology</td><td>Reference for BRY07 and BRY01</td></tr>
<tr><td>ANSOURCE</td><td rowspan="2">Point sources (sinks) of water volume (0.5 Sv in total) with background T and S introduced in upwelling active regions between the depth range of 500 to 1000 m</td><td rowspan="6">Exert upwelling convergence (divergence) in selected regions</td></tr>
<tr><td>ANSINK</td></tr>
<tr><td>SOURCENOT</td><td rowspan="4">Point sources (sinks) of water volume (0.5 Sv in total) with background T and S introduced in northern (southern) Okinawa Trough between the depth range of 500 to 1000 m</td></tr>
<tr><td>SINKNOT</td></tr>
<tr><td>SOURCESOT</td></tr>
<tr><td>SINKSOT</td></tr>
<tr><td>FPLANE</td><td>Uniform f inside the Okinawa Trough</td><td>Turn of planetary β effect inside the Okinawa Trough</td></tr>
</table>

Compared with BRYAN, when the deep OT experience a positive (negative) PV influx, as evident in cases BRY07 (BRY01), a cyclonic (anticyclonic) circulation anomaly emerges along the OT boundary (refer to Figure 8a and 8b). This consensus is quantitively illustrated in Figure 8c and 8d. The annual mean PV flux into the OT is 0.071 m^2s^{-2} in the BRYAN case. In BRY07, however, the net PV flux increases to 0.095 m^2s^{-2}, while in BRY01, the net PV flux decreases to 0.050 m^2s^{-2}. The LF torque correspondingly increases to 0.091 m^2s^{-2} in BRY07 case while decreases to 0.056 m^2s^{-2} in BRY01 case, indicating the adjustment of the deep circulation. Note that LF torque terms in all three runs are calculated using the same regressed λ. The 1-month lead-lag correlation still holds in both BRY07 and BRY01 because the damping of this system remains intact in these cases. Therefore, the robustness of the PV budget is verified by these experiments.

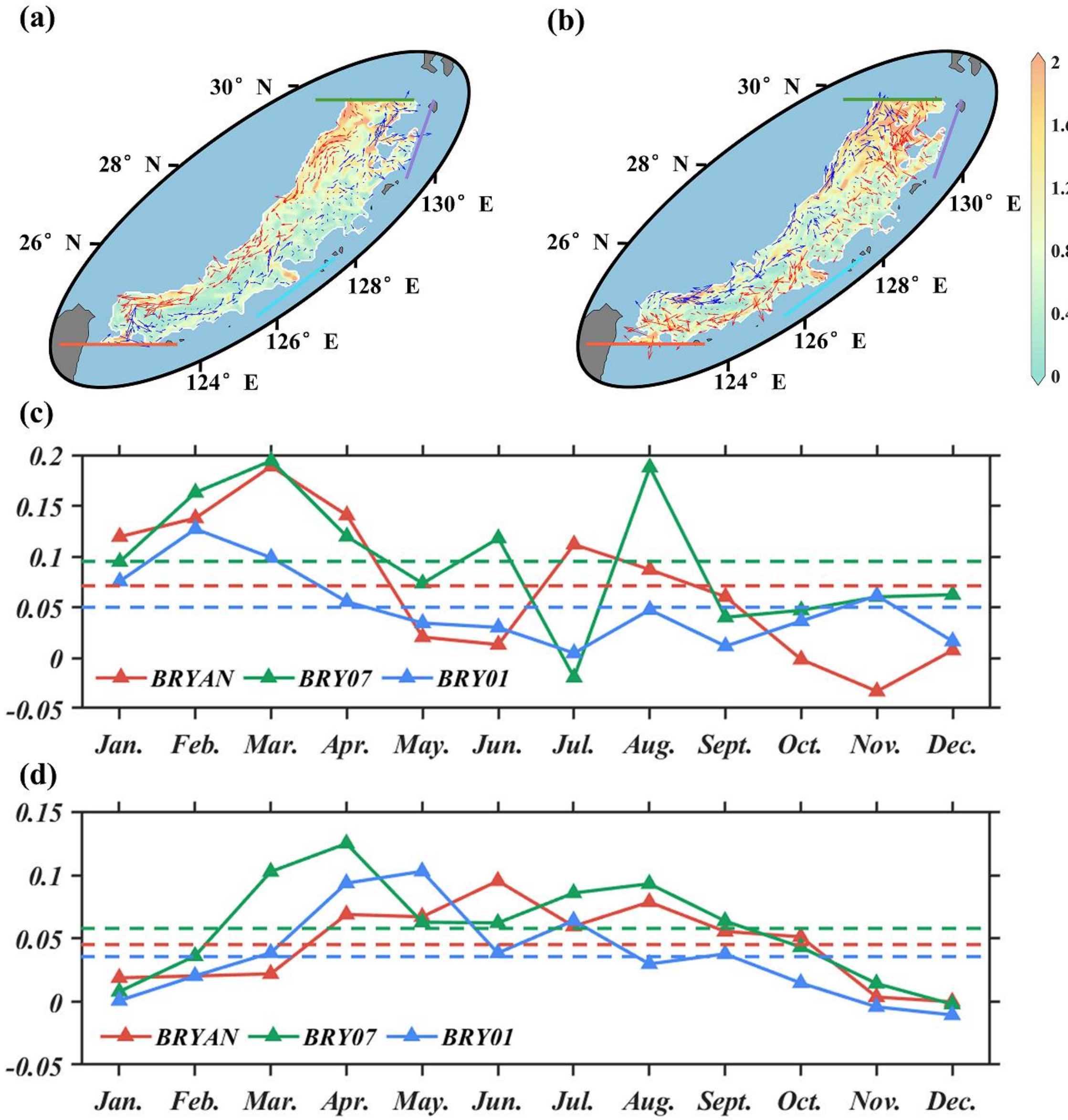

Figure 8. The PV constraint in the Okinawa Trough. **(a)** The difference between case BRY07 and case BRYAN. The arrows denote the annual mean bottom-layer velocity anomaly (red for southwestward and blue for northeastward), and the shading denotes velocity anomaly magnitude. The velocity anomaly weaker than 0.1 cm s^{-1} is masked. **(b)** Same as Figure 8a, but for the difference between BRY01 and BRYAN. **(c)** The monthly mean net PV flux into the Okinawa Trough. **(d)** Same as Figure 8c, but for the LF torque. PV, potential vorticity; LF torque, lateral frictional torque.

4.2 **Onshore intrusion and upwelling divergence**

Although the validity of PV constraint in the deep OT is demonstrated, it is yet not clear why the net PV influx is always positive and induces a cyclonic circulation pattern. In this section, we address that the divergence of upwelling, which mostly results from the onshore intrusion of the deep water, is the driving factor for the SCC formation.

The ECS slope has been widely documented as a location where onshore intrusions of Kuroshio water occur, characterized by high-salinity and nutrient-rich content (Hu et al., 2020;

Wei, 2018; Yang et al., 2018; Gan et al., 2016; Isobe and Beardsly, 2006). Onshore intrusion refers to the movement of water particles towards shallower regions and is invariably accompanied by vertical displacements of their altitudes. The vertical displacements of water particles are evident in the drifter trajectories, which are categorized into three typical types in Figure 9. Type 1 signifies the active onshore intrusion at the central part of the ECS slope. The drifters in for type 1 are initialized at the northern slope of the OT, carried southwestward by the SCC, and intrude onto the ECS shelf around 127°E, 27.5°N. An abrupt change in the altitudes of drifters are observed within 30 days (from day 180 to day 210) in the right panel. Type 2 is not a categorize for the onshore intrusion of Kuroshio, but rather a case for vertical movement of water particles advected by the strong upwelling over the zonally running shelf break northeast of the Taiwan Island. The vigorous onshore intrusion northeast of the Taiwan Island is accurately captured the drifter trajectories, specifically denoted as type 3 in the bottom panel of Figure 9, which show similar patterns to previous studies.

Time-varying tracer 2 concentration in Figure 10 serves as one of the pieces of evidence for the upward lift of water particles as well. The water column inside the OT at the SCC layer is dyed with tracer 2 with a fixed 100 kg m^{-3} concentration. After 70 days, the penetration of SCC-layer water onto the ECS is apparent, mainly through the paths illustrated above. It is worth mentioning that nearly 90% of the ECS is covered with tracer 2, which originates from the depth range of 500 to 1000 meters inside the OT. Therefore, the ESOM simulation shows that the SCC plays a surprisingly crucial role in shaping the hydrological environment of the ECS.

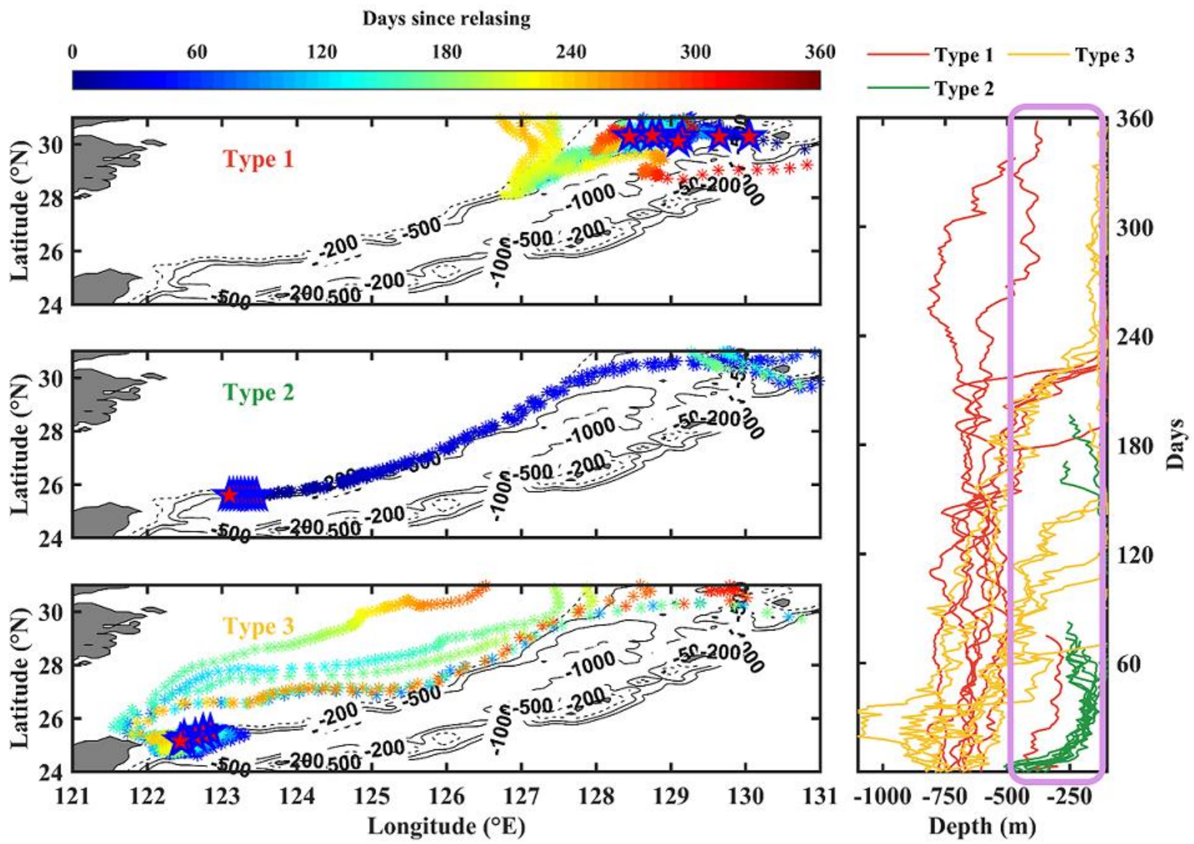

Figure 9. Different types of drifter trajectories which reveal the water particles from the depth of SCC layer transported to the upper layer. The left three panels illustrate the locations of these drifters. The right panel displays their time-evolving depths, with the 0 to 500-meter depth range marked by a purple rectangle. These drifters are recorded every 36 hours.

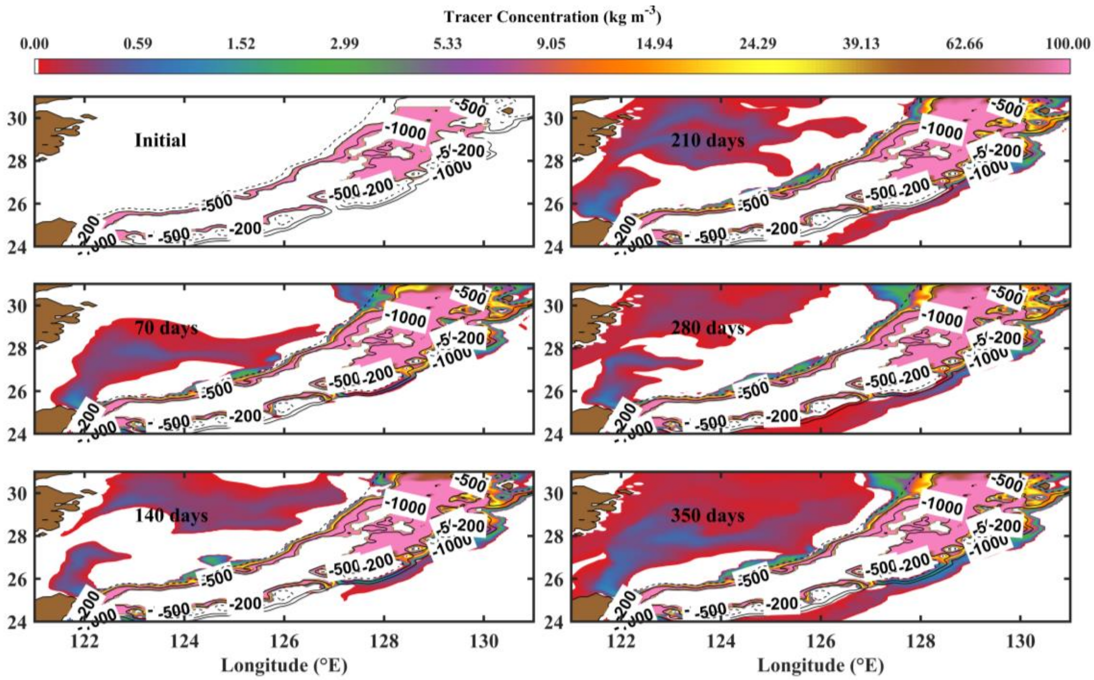

Figure 10. Time-varying tracer concertation at the bottom terrain-following layer for tracer 2. The dashed line represents the 200-meter isobaths, while the 500-meter and 1000-meter isobaths are indicated by solid lines.

The vertical displacements of water particles lead to upwelling divergence in the SCC layer, necessitating lateral volume (LV) influx to compensate. In the ESOM simulation, vertical motions at the 500-m depth are most active over the ECS slope (see Figure 11a), and their distribution conforms to a typical onshore intrusion pattern observed in previous studies (e.g., Figure 6b in Hu et al., 2020). Relative to the vertical motions observed at the 500-meter depth in Figure 11a, those at the 1000-meter depth are much less active, as depicted in Figure 11c. Across the entire OT, the SCC layer experiences an annual loss of 0.50 Sv at the 500-meter depth and gains 0.18 Sv at the 1000-meter depth. This results in a net loss of 0.32 Sv vertically, contributing to a divergent SCC layer. Notably, it is reported by Zhang et al. (2017) that the bottom-layer cross-shelf transport into the ECS shelf in the sloping regions is about 0.7 Sv, which is comparable with the 0.5 Sv in our case. In an annual mean state, the loss of water volume is expected to be compensated by LV influxes through T1~T4 since ROMS conserves volume. The ESOM anticipates that there is a net LV influx of 0.2 Sv annually into the SCC layer of OT. Although the net LV influx is not a perfect match for the loss of volume from the upwelling divergence, this result is totally understandable considering the uncertainty in interpolation.

Assuming the water through the breaches conserves volume and advects constant PV, equation 1 can be reformulated through the divergence theorem as:

$$(W_1 - W_2)\frac{f_0}{H_0} = -\lambda \oint_C (\boldsymbol{u_h} \cdot \boldsymbol{l})\, ds + Res \qquad (2)$$

where W_1 and W_2 are respectively the vertical volume fluxes at the upper layer and lower layer (500 m and 1000 m in this case), f_0/H_0 denotes the constant PV. Equation (2) means upwelling divergence induces positive PV inflow and hence results in the cyclonic circulation. Figure 11c shows the net PV flux term $\sum_{i=1}^{N} Q_i f_i / H_i$, is closely related to the net volume flux. It indicates the different PVs at the OT breaches, f_i/H_i, can be regarded as constant f_0/H_0. The net PV flux is hence largely determined by the net LV flux, which provides evidence for the assumption in equation (2).

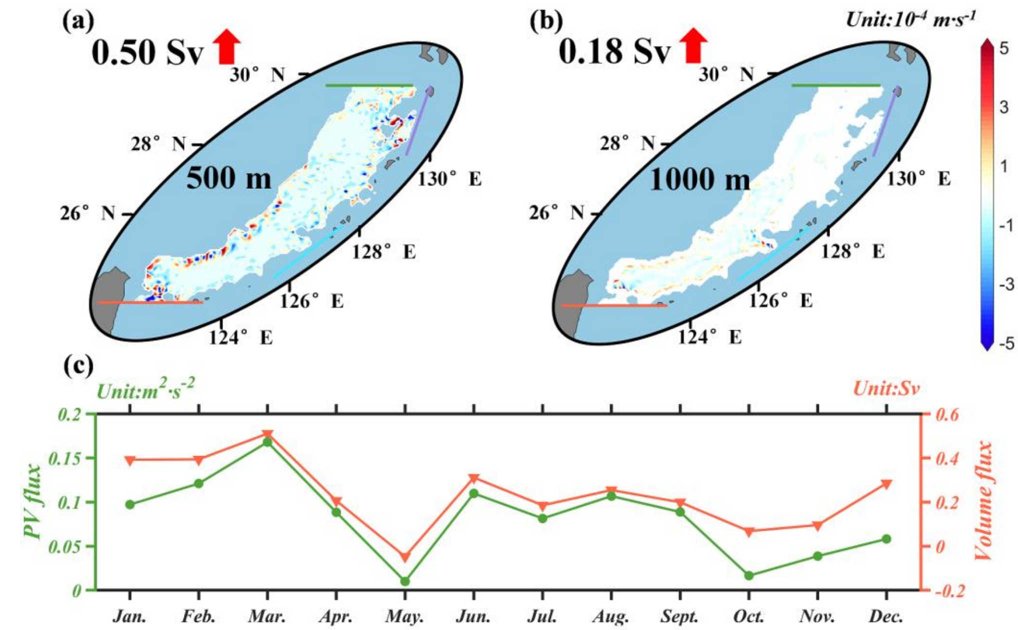

Figure 11. Upwelling divergence and lateral fluxes in the deep Okinawa Trough. **(a)** Annually averaged vertical velocity at 500-m depth. Regions shallower than 500m or out of the Okinawa Trough are masked by blue shading. **(b)** Same as Figure 11a, but for the vertical velocity at 1000-m depth. **(c)** The monthly mean net PV influx (in green) and lateral volume influx into the Okinawa Trough (500 to 1000 m).

Subsequently, two experiments (case ANSOURCE and case ANSINK) are additionally conducted to show that the upwelling divergence indeed manipulates the boundary circulation in the SCC layer. In case ANSOURCE (ANSINK), a total amount of 0.5 Sv point source (sink) is introduced along the ECS slope between 500 to 1000 m to alter the upwelling divergence in the SCC layer. As anticipated, Figure 12a (12b) illustrates a notable anticyclonic (cyclonic) circulation anomaly in the northern OT, accompanied by reduced (increased) LV influxes through the breaches. The changes in LV influx in ANSOURCE and ANSINK are most significant through the Kerama Gap, indicating the unique importance of this deep channel in regulating the deep circulation in the OT. In Figure 12a, these noteworthy velocity anomalies are primarily concentrated in the vicinity of the applied source (sink) regions. This can be explained as follows: the lateral volume (LV) flux acts to offset the effects of the extra sources and sinks, causing alterations in local PV. As a result, bottom friction responds by adjusting the boundary flow to eliminate these changes. We have also switched the locations of these sources (sinks) in other locations (case SOURCENOT, SINKNOT, SOURCESOT, and SINKSOT, refer to Table 1), the results of which point to a single answer as expected (Figure 12c~f) although they exhibits some detailed differences.

Based on the analyses above, we conclude that the upwelling divergence in the OT is the driving factor for the trough-scale slope countercurrent.

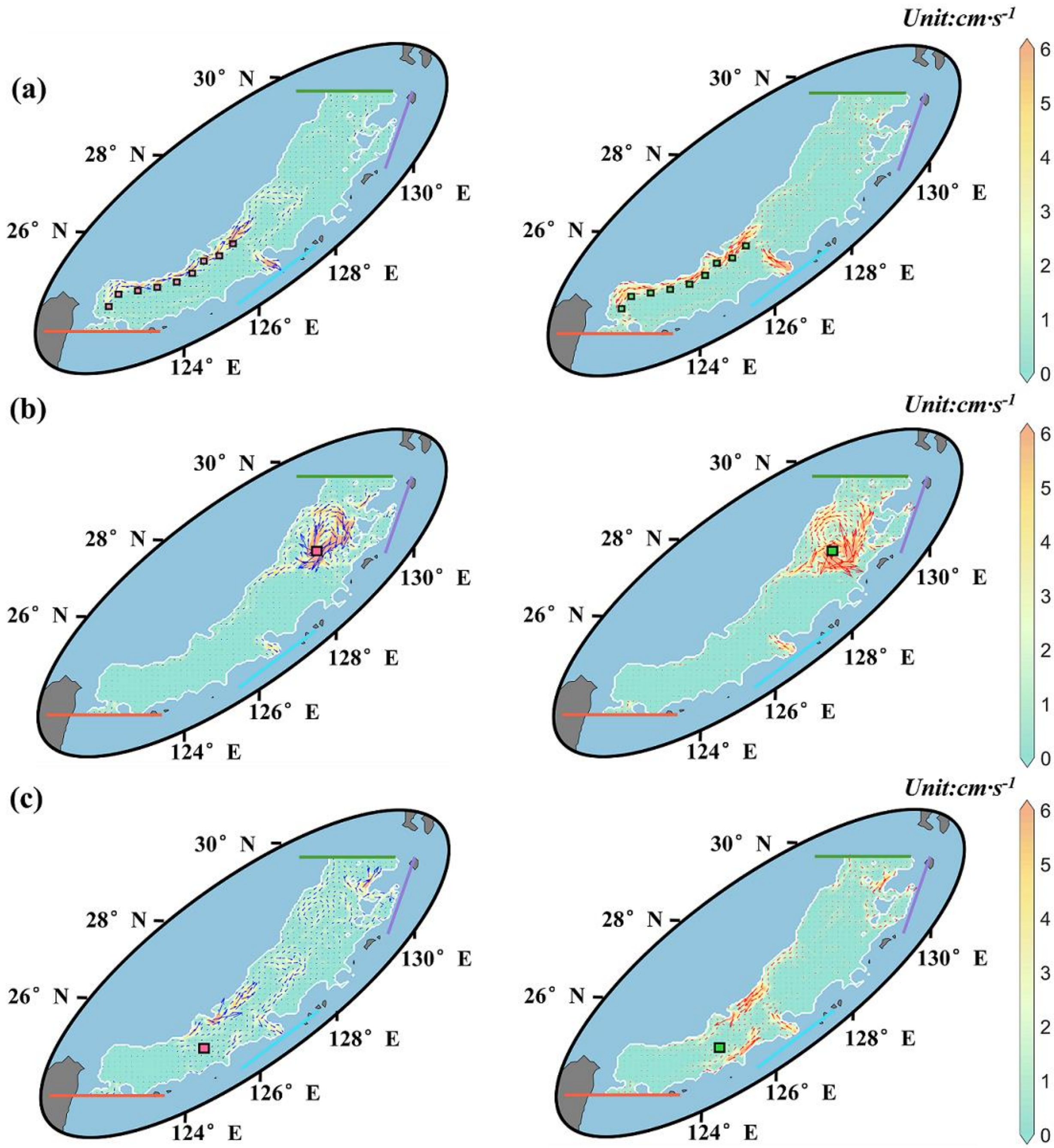

Figure 12. Circulation anomalies from source and sink experiments. **(a)** The difference between case ANSOURCE and the control run in the left panel, and in the right panel the difference between case ANSINK and the control run. **(b)** Same as Figure 12a, but for the results of case SOURCENOT and SINKNOT. **(c)** Same as Figure 12a, but for the results of SOURCESOT and SINKSOT. Blue arrows depict anticyclonic anomalies, while red arrows signify cyclonic anomalies. Red rectangles denote point sources of water volume, while the green ones represent the opposite.

5 Discussions

5.1 SCC contributes to the Kuroshio onshore intrusion

The SCC over the ECS shelf break is in a sense a boundary flow that counters the surface Kuroshio. From a trough-scale perspective, this continuous countercurrent may potentially have a profound influence on mass, heat, and nutrient transport. The Kuroshio onshore intrusion northeast of the Taiwan Island has been extensively investigated in the past decade. There is a near-consensus that the surface Kuroshio water and the Kuroshio subsurface water are the main sources of the intruded water. However, this study brings new insight into this vigorous intrusion event in that the SCC over the ECS shelf break also contributes to the penetration. The time-varying concentration of tracer 1 reveals that the water mass in the northern part of the deep OT is consistently transported by the SCC from the initiation. After 560 days, tracer 1 covers the entire ocean bottom in the OT. This northern-OT-originated tracer penetrates into the East China Sea through the characteristic onshore intrusion path northeast of the Taiwan Island after 700 days.

The OT is known as an active place for hydrothermal vents and cold seeps which transfer and exchange materials and energies. As the SCC is positioned directly over the ECS shelf break and exhibits bottom intensification, it is highly probable that sediment distribution OT is profoundly influenced by it. When connected with the active upwelling near the ECS slope, the SCC may also play a vital role in maintaining regional biodiversity, and the ESOM simulation above serves as supporting evidence.

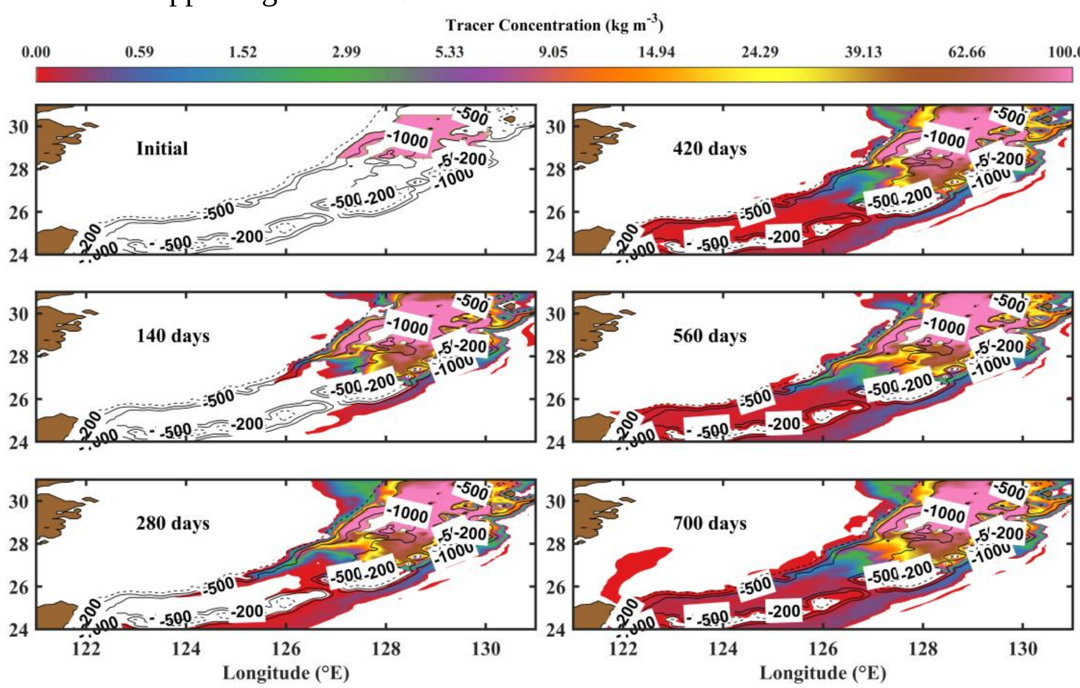

Figure 13. Time-varying tracer concertation at the bottom terrain-following layer for tracer 1. The dashed line represents the 200-meter isobaths, while the 500-meter and 1000-meter isobaths are indicated by solid lines.

5.2 **Westward intensification**

Another intriguing feature is the westward intensification of this cyclonic circulation. The western intensification of ocean circulations is attributed to the β effect (Stommel, 1948; Munk, 1950) where β is the meridional gradient of the Coriolis parameter f. The OT is an elongated basin with a relatively small zonal width. Its shape and depth are strongly influenced by bathymetry. It is plausible that circulations in the OT are affected more profoundly by the topographic β than the planetary β.

We design and conduct an additional experiment (FPLANE case, refer to Table 1) in which f is uniform within the OT but varies with latitudes elsewhere. The main purpose is to examine whether or how circulations in the OT are affected locally by the planetary β (see Figure 14a for the distribution of f). The annual mean magnitudes of the tangential velocity $M = \boldsymbol{u_h} \cdot \boldsymbol{l}$ along the western boundary and the eastern boundary of the OT (M_w and M_e) at the 800-m depth are calculated (refer to Figure 14b). The intensification ratio r is defined as the ratio of M_w divided by M_e. In the control run, the intensification ratio is about 3.9 (see Figure 14c). For the FPLANE case, the ratio r sharply decrease to 2.2 when the planetary β effect in the OT is removed (see Figure 14d), suggesting the planetary β contributes most of the westward intensification feature. The rest part of the westward intensification may potentially be attributed to topographic β (the meridional bathymetry gradient in the OT) and the discontinuity and complexity of the eastern OT boundary.

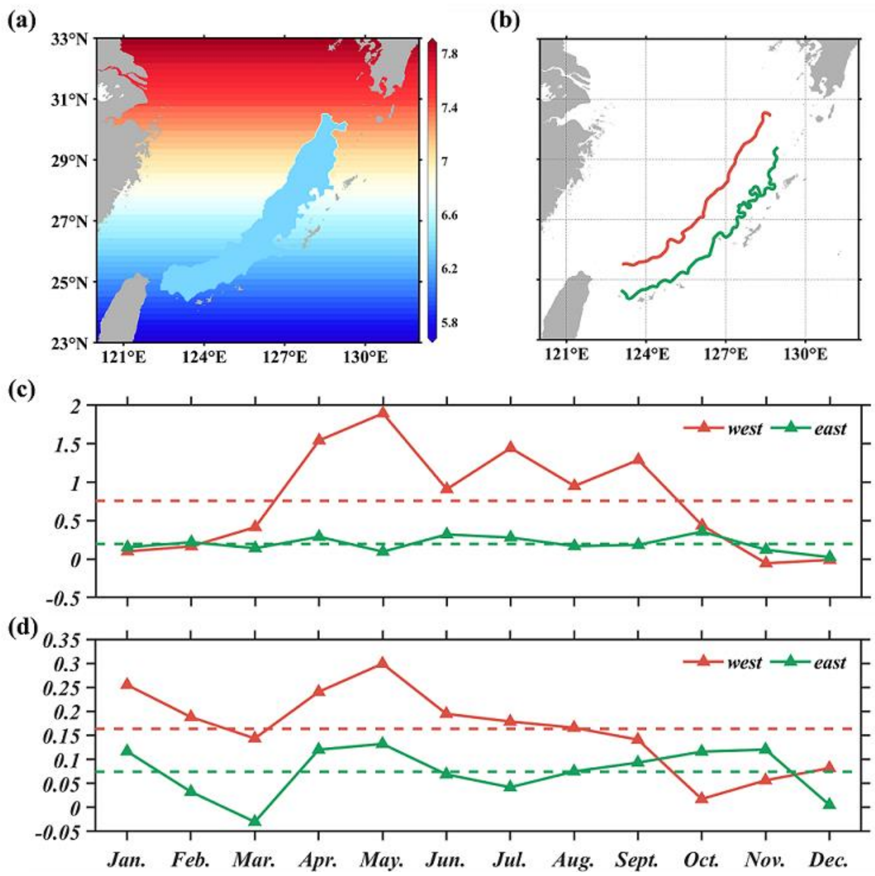

Figure 14. Westward intensification feature in the Okinawa Trough. **(a)** The Coriolis parameter configuration in the *f*-plane case, in which *f* is set to uniform within the OT. **(b)** The western and eastern boundaries along which the mean tangential velocity at the 800-m depth are calculated, red for the western OT boundary, green for the eastern OT boundary. **(c)** Monthly mean circulation intensity in the control run, red for

the western part, green for the eastern part. The annual mean values are marked with dashed lines. Unit: cm s^{-1}. **(d)** Same as Figure 14c, but for *f*-plane case.

The dynamical process we illustrated in this study may potentially be universal in western boundary regions with sloping bottoms because the bottom stress, which determines the bottom Ekman transport, is large and varies significantly with depth in sloping bottoms. The convergence and divergence of bottom Ekman transport in the sloping region will induce lateral volume fluxes which advect PV and drive the sense boundary flow.

6 Conclusions

We focus on the SCCs revealed by historical observations at different sites over the ECS shelf break. The SCCs have long been regarded as parts of the cyclonic eddies in the northern OT. Our study reveal that the SCC is associated with a continuous OT-wide cyclonic circulation. The trough-scale circulation in the lower-layer OT is primarily driven by upwelling divergence. In the sloping region, the divergence of upwelling induces lateral volume fluxes that advects PV mainly through three transects. In annual mean climatology, volume fluxes of 1.35 Sv and 0.48 Sv enter the OT through the passage over the ETC and the Kerama Gap respectively. A lower-layer volume flux of 1.63 Sv leaves the OT through the Tokara Strait. These three fluxes together result in a positive net PV flux of 0.082 m^2s^{-2} into the lower-layer OT, which requires negative LF torque to balance it and therefore a trough-scale cyclonic circulation exits along the OT boundary. This process is illustrated by a schematic in Figure 15. This circulation pattern is clearly depicted in the well-validated ESOM simulations. The SCC is weak but stable with a mean magnitude of $O(1)\ cm \cdot s^{-1}$, much weaker compared to the Kuroshio Current which lies over it. It is also found that the SCC substantially contributes to the onshore intrusion northeast of the Taiwan Island, providing a new perspective for comprehending the intricate circulation patterns in the northwest Pacific Ocean.

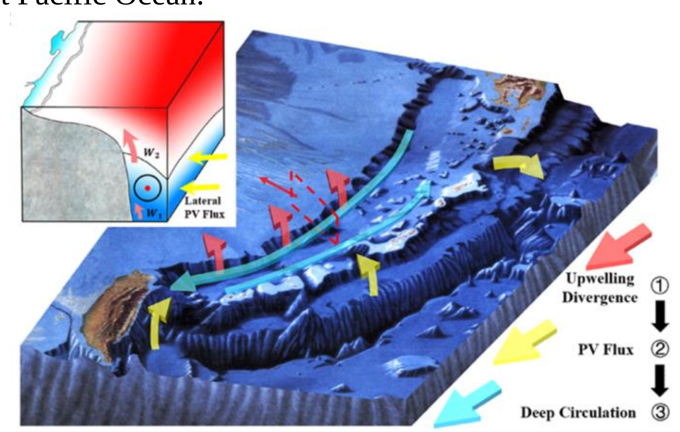

Figure 15. Schematic of the formation mechanism of the slope countercurrent over the East China Sea shelf break.

In this study, we demonstrate the mechanism for the SCC using a numerical model and physical interpretations. Understanding the formation mechanism of the SCC is greatly beneficial for identifying its role in the regional climate, geology, and ecosystem. More observations are needed to quantify the spatial and temporal variations in the lower-layer cyclonic circulation in the OT, especially the SCC beneath the Kuroshio Current. More attention to the SCC variability and its connection to the surface Kuroshio is called for in future research.

Acknowledgments

This study was supported by the National Natural Science Foundation of China (Nos. 42076022 and 92158202), the Strategic Priority Research Program of the Chinese Academy of Sciences (Nos. XDB42000000 and XDA19060203), the National Key Research and Development Plan Sino-Australian Center for Healthy Coasts (No. 2016YFE0101500) and the CAS-CSIRO BAU project (No. 133137KYSB20180141). It was also supported by the High Performance Computing Center at the IOCAS, East China Sea ocean observation and research station of OMORN, and the Youth Innovation Promotion Association CAS. Arthur J. Miller was partly supported by the National Science Foundation (OCE-2022868). Thanks for the data service provided by the Oceanographic Data Center, Chinese Academy of Sciences(CASODC)(http://msdc.qdio.ac.cn)

Open Research

The model set-up in this paper are available at https://doi.org/10.1016/j.pocean.2018.08.004. The data used to reproduce the results of this paper are available at 10.6084/m9.figshare.24602691.

References

Andres, M., Jan, S., Sanford, T., Mensah, V., Centurioni, L., & Book, J. (2015). Mean structure and variability of the Kuroshio from northeastern Taiwan to southwestern Japan. *Oceanography*, 28(4), 84– 95. https://doi.org/10.5670/oceanog.2015.84

Andres, M. , Wimbush, M. , Park, J. H. , Chang, K. I. , Lim, B. H. , & Watts, D. R. , et al. (2008). Observations of Kuroshio flow variations in the East China Sea. *Journal of Geophysical Research: Oceans*, 113(C5). https://doi.org/10.1029/2007JC004200

Beal, L. M. , & Bryden, H. L. . (1997). Observations of an AgulhasUndercurrent. *Deep Sea Research, Part I: Oceanographic Research Papers*, 44(9-10), 1715-1724. https://doi.org/10.1016/S0967-0637(97)00033-2

Beckmann, A., and D. B. Haidvogel. (1993). Numerical simulation of flow around a tall isolated seamount, 1, Problem formulation and model accuracy, *Journal of Physical. Oceanography*, 23(8), 1736–1753. https://doi.org/10.1175/1520-0485(1993)023<1736:NSOFAA>2.0.CO;2

Chen, X. , & Tung, K. K. . (2018). Global surface warming enhanced by weak Atlantic overturning circulation. *Nature*, 559, 387-391. https://doi.org/10.1038/s41586-018-0320-y

Cui, X., Yang, D., Sun, C., Feng, X., Gao, G., Xu, L., & Yin, B. (2021). New insight into the onshore intrusion of the Kuroshio into the East China Sea. *Journal of Geophysical Research: Oceans*, 126, e2020JC016248. https://doi.org/10.1029/2020JC016248

Dee, D.P., et al., (2011). The ERA-Interim reanalysis: configuration and performance of the data assimilation system. *Quarterly Journal of the Royal Meteorological Society*. 137 (656), 553–597. https://doi.org/10.1002/Qj.828.

Diaz, H., C. Folland, T. Manabe, D. Parker, R. Reynolds, and S. Woodruff. (2002). Workshop on advances in the use of historical marine climate data. *World Meteorology*. Org. Bull., 51, 377–380.

Dinniman, M. S., Klinck, J. M., & Smith, W. O. (2003). Cross-shelf exchange in a model of the Ross Sea circulation and biogeochemistry. *Deep Sea Research Part II: Topical Studies in Oceanography*, 50(22–26), 3103-3120. https://doi.org/10.1016/j.dsr2.2003.07.011

Egbert, G.D., Erofeeva, S.Y., (2002). Efficient inverse modeling of barotropic ocean tides. *Journal of Atmospheric and Oceanic Technology*. 19 (2), 183–204. https://doi.org/10.1175/1520-0426(2002)019<0183:Eimobo>2.0.Co;2.

Gan, J. P., Liu, Z. Q., and Liang, L. L. (2016). Numerical modeling of intrinsically and extrinsically forced seasonal circulation in the China Seas: a kinematic study. *Journal of Geophysical Research: Oceans*, 121, 4697-4715. https://doi.org/10.1002/2016jc011800

Gula, J., Molemaker, M. J., & Mcwilliams, J. C. (2015). Gulf Stream dynamics along the southeastern U.S. seaboard. *Journal of Physical Oceanography*, 45(3), 690– 715. https://doi.org/10.1175/JPO-D-14-0154.1

Haney, R. L.(1991). On the pressure gradient force over steep topography in sigma coordinate ocean models, *Journal of Physical Oceanography*, 21, 610–618. https://doi.org/10.1175/1520-0485(1991)021<0610:OTPGFO>2.0.CO;2

Hu, F., Liu, Y., Xu, Z., Yin, Y., & Hou, Y.. (2020). Bidirectional volume exchange between kuroshio and east china sea shelf water based on a whole - region passive - tracing method. *Journal of Geophysical Research: Oceans*, 125(5). https://doi.org/10.1029/2019JC015528

Huang, R. X. , & Yang, J. . (1996). Deep-water upwelling in the frictional western boundary layer. *Journal of Physical Oceanography*, 26(10), 2243-2250. https://doi.org/10.1175/1520-0485(1996)026<2243:DWUITF>2.0.CO;2

Isobe, A. and Beardsley, R. C. . (2006). An estimate of the cross-frontal transport at the shelf break of the East China Sea with the Finite Volume Coastal Ocean Model. *Journal of Geophysical Research: Oceans*, 111(C3). https://doi.org/10.1029/2005JC003290

Kuhlbrodt, T. , Griesel, A. , Montoya, M. , Levermann, A. , Hofmann, M. , & Rahmstorf, S. . (2007). On the driving processes of the Atlantic meridional circulation. *Reviews of Geophysics*, 45(2). https://doi.org/10.1029/2004RG000166

James, C., M. Wimbush, and H. Ichikawa (1999), Kuroshio meanders in the East China Sea, *Journal of Physical Oceanography*, 29, 259-272. https://doi.org/10.1175/1520-0485(1999)029<0259:KMITEC>2.0.CO;2

Karcher, M., Kauker, F., Gerdes, R. , Hunke, E. , & Zhang, J. . (2007). On the dynamics of atlantic water circulation in the arctic ocean. *Journal of Geophysical Research: Oceans*, 112(C4). https://doi.org/10.1029/2006JC003630

Lie, H.-J., C.-H. Cho, and A. Kaneko (1998), On the branching of the Kuroshio and the formation of slope countercurrent in the East China Sea, paper presented at Japan-China Joint Symposium on Cooperative Study of Subtropical Circulation System, Seikai Natl. Fish. Res. Inst., Naha, Japan.

Marchesiello, P., McWilliams, J. C., & Shchepetkin, A. (2003). Equilibrium structure and dynamics of the California Current System. *Journal of Physical Oceanography*, 33(4), 753– 783. https://doi.org/10.1175/1520-0485(2003)33<753:ESADOT>2.0.CO;2

Nakamura, H. (2005). Numerical study on the Kuroshio path states in the northern Okinawa Trough of the East China Sea, *Journal of Geophysical Research Oceans*,110, C04003. https://doi.org/10.1029/2004JC002656 doi:10.1029/2004JC002656.

Nakamura, H., H. Ichikawa, A. Nishina, and Lie H. (2003). Kuroshio path meander between the continental slope and the Tokara Strait in the East China Sea, *Journal of Geophysical Research Oceans*, 108(C11), 3360, https://doi.org/10.1029/2002JC001450

Nakamura, H., Nishina A., Ichikawa, H., Nonaka, M., Sasaki, H.. (2008). Deep countercurrent beneath the Kuroshio in the Okinawa Trough. *Journal of Geophysical Research Oceans*. https://doi.org/10.1029/2007JC004574

Peliz, A., Dubert, J. S., & Haidvogel, D. B. (2003). Subinertial response of a density-driven eastern boundary poleward current to wind forcing. *Journal of Physical Oceanography*, 33(8), 1633-1650. https://doi.org/10.1175/2415.1

Qiu, B., & Imasato, N. (1990). A numerical study on the formation of the Kuroshio Counter Current and the Kuroshio Branch Current in the East China Sea. *Continental Shelf Research*, 10(2), 165– 184. https://doi.org/10.1016/0278-4343(90)90028-K

Shchepetkin, A. F., & McWilliams, J. C. (2005). The regional oceanic modeling system (ROMS): A split-explicit, free-surface, topography-following-coordinate oceanic model. *Ocean Modelling*, 9(4), 347– 404. https://doi.org/10.1016/j.ocemod.2004.08.002

Song, Y., & Haidvogel, D. (1994). A semi-implicit ocean circulation model using a generalized topography-following coordinate system. *Journal of Computational Physics*, 115(1), 228– 244. https://doi.org/10.1006/jcph.1994.1189

Stommel, H. M. . (1948). The western intensification of wind-driven ocean currents. *Eos Transactions American Geophysical Union*, 29. https://doi.org/10.1029/TR029i002p00202

Stommel, H. 1958. The abyssal circulation. Deep-Sea Res., 5, 80–82. https://doi.org/10.1016/S0146-6291(58)80014-4

Stommel, H. and A. B. Arons. 1960a. On the abyssal circulation of the world ocean. I. Stationary planetary flow patterns on a sphere. *Deep-Sea Res*., 6, 140–154. https://doi.org/10.1016/0146-6313(59)90065-6

— 1960b. On the abyssal circulation of the world ocean. II. An idealized model of the circulation pattern and amplitude in oceanic basins. *Deep-Sea Res*., 6, 217–233. https://doi.org/10.1016/0146-6313(59)90065-6

Sun, Y. , Clemens, S. C. , Morrill, C. , Lin, X. , Wang, X. , & An, Z. . (2012). Influence of Atlantic meridional overturning circulation on the east Asian winter monsoon. *Nature Geoscience*, 5(1), 46-49. https://doi.org/10.1038/ngeo1326

Lan, J. , Zhang, N. , & Wang, Y. . (2013). On the dynamics of the South China Sea deep circulation. *Journal of Geophysical Research Oceans*, 118(3), 1206-1210. https://doi.org/10.1002/jgrc.20104

Toole, J. M., M. Andres, I. A. Le Bras, T. M. Joyce, and M. S. McCartney, 2017: Moored observations of the Deep Western Boundary Current in the NW Atlantic: 2004–2014. *Journal of Geophysical Research Oceans*, 122, 7488–7505, https://doi.org/10.1002/2017JC012984.

Lynne, D. , & Talley. (2008). Freshwater transport estimates and the global overturning circulation: shallow, deep and throughflow components. *Progress in Oceanography*, 78(4), 257-303. https://doi.org/10.1016/j.pocean.2008.05.001

Warren, B. A., & Speer, K. G. (1991). Deep circulation in the eastern south Atlantic Ocean. *Deep Sea Research-Part A:Oceanographic Research Papers*, 38(S1), S281-S322. https://doi.org/10.1016/S0198-0149(12)80014-8

Wunsch, C. , & Ferrari, R. . (2003).Vertical mixing, energy, and the general circulation of the oceans. *Annual Review of Fluid Mechanics*, 36, 281-314. *Annual Review of Fluid Mechanics*, 18(36), 281-314. https://doi.org/10.1146/annurev.fluid.36.050802.122121

Yang, D., Huang, R., Feng. X., Qi. J., Gao. G., & Yin. B (2020). Wind stress over the Pacific Ocean east of Japan drives the shelf circulation east of China. *Continental Shelf Research*, 201. https://doi.org/10.1016/j.csr.2020.104122

Yang, D., Huang, R., Yin, B. ,Feng, X., Chen, H., Qi, J., Benthuysen, J. (2018)a. Topographic beta spiral and onshore intrusion of the Kuroshio Current. Geophysical Research Letters, 45, 287–296. https://doi.org/10.1002/2017GL076614

Yang, D., Yin, B., Chai, F., Feng, X., Xue, H., Gao, G., & Yu, F. (2018b). The onshore intrusion of Kuroshio subsurface water from February to July and a mechanism for the intrusion variation. *Progress in Oceanography*, 167, 97-115. https://doi.org/10.1016/j.pocean.2018.08.004

Yang, J. , & Price, J. F. . (2000). Water-mass formation and potential vorticity balance in an abyssal ocean circulation. *Journal of Marine Research*, 58(5), 789-808. https://doi.org/10.1357/002224000321358918

Yang, J. . (2005). The arctic and subarctic ocean flux of potential vorticity and the arctic ocean circulation. *Journal of Physical Oceanography*, 35(12), 2387. https://doi.org/10.1175/JPO2819.1

Yang, J. , & Price, J. F.. (2007). Potential Vorticity Constraint on the Flow between Two Basins. *Journal of Physical Oceanography*, 37(9), 2251–2266. https://doi.org/10.1175/JPO3116.1

Zhang, J. , Zhao, L. , Guo, X. , & Miyazawa, Y. . (2017). Water exchange across isobaths over the continental shelf of the East China Sea. *Journal of Physical Oceanography*, 47(5), 1043-1060. https://doi.org/10.1175/JPO-D-16-0231.1

Zhu, Y. , Sun, J. , Wang, Y. , Wei, Z. , Yang, D. , & Qu, T. . (2017). Effect of potential vorticity flux on the circulation in the South China Sea. *Journal of Geophysical Research Oceans*. 122(8), 6454-6469. https://doi.org/10.1002/2016JC012375

Zhu, Y., Wang, L., Wang, Y., Xu, T., Li, S., Cao, G., Wei, Z., Qu, T. . (2019). Stratified circulation in the Banda Sea and its causal mechanism. *Journal of Geophysical Research: Oceans*. 124(10), 7030-7045. https://doi.org/10.1029/2019JC015279

Figure 1.

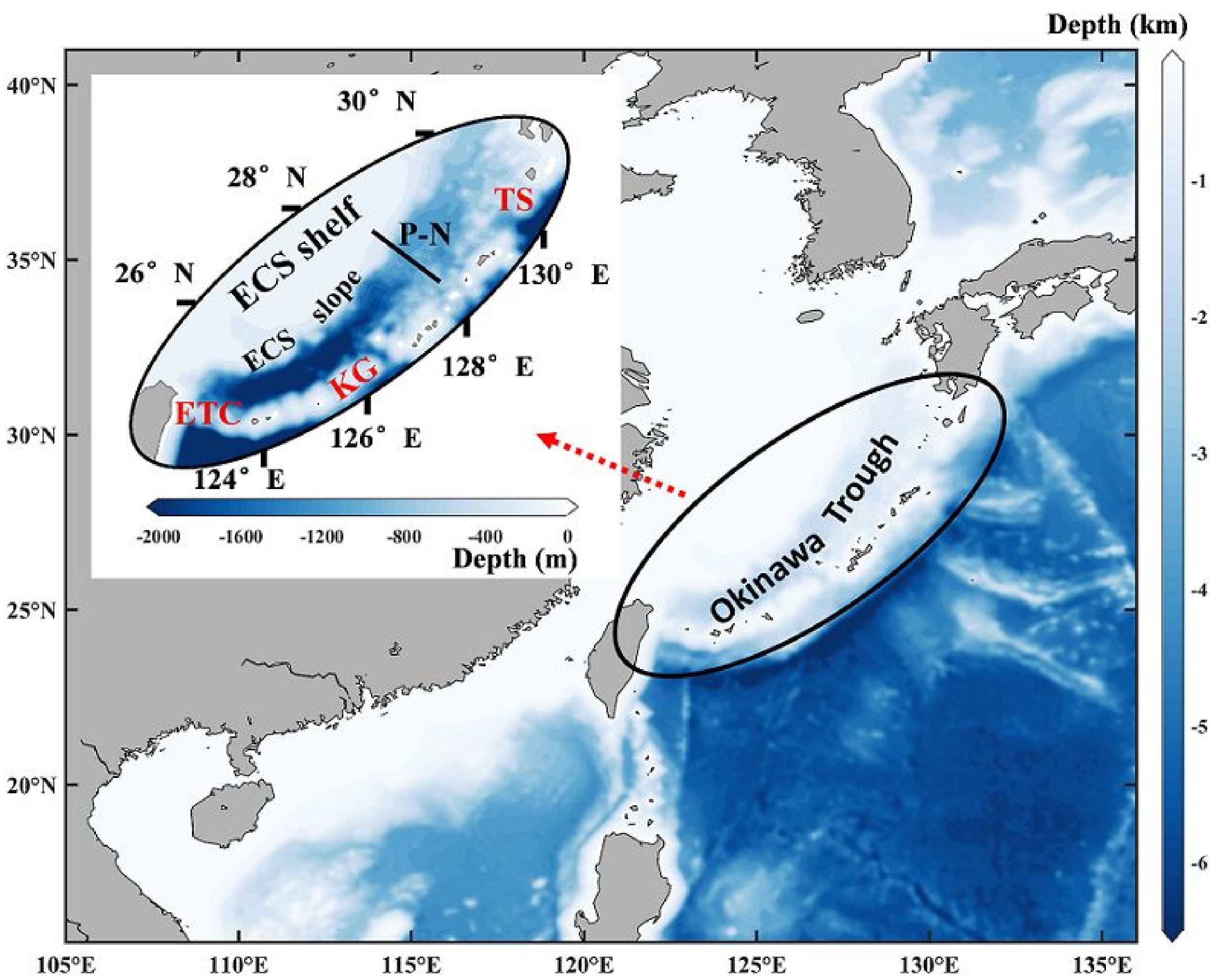

Depth (km)
-1
-2
-3
-4
-5
-6
40°N
35°N
30°N
25°N
20°N
105°E
110°E
115°E
120°E
125°E
130°E
135°E
Okinawa Trough
30° N
28° N
26° N
ECS shelf
ECS slope
ECS
P-N
TS
KG
ETC
130° E
128° E
126° E
124° E
-2000
-1600
-1200
-800
-400
0
Depth (m)

Figure 2.

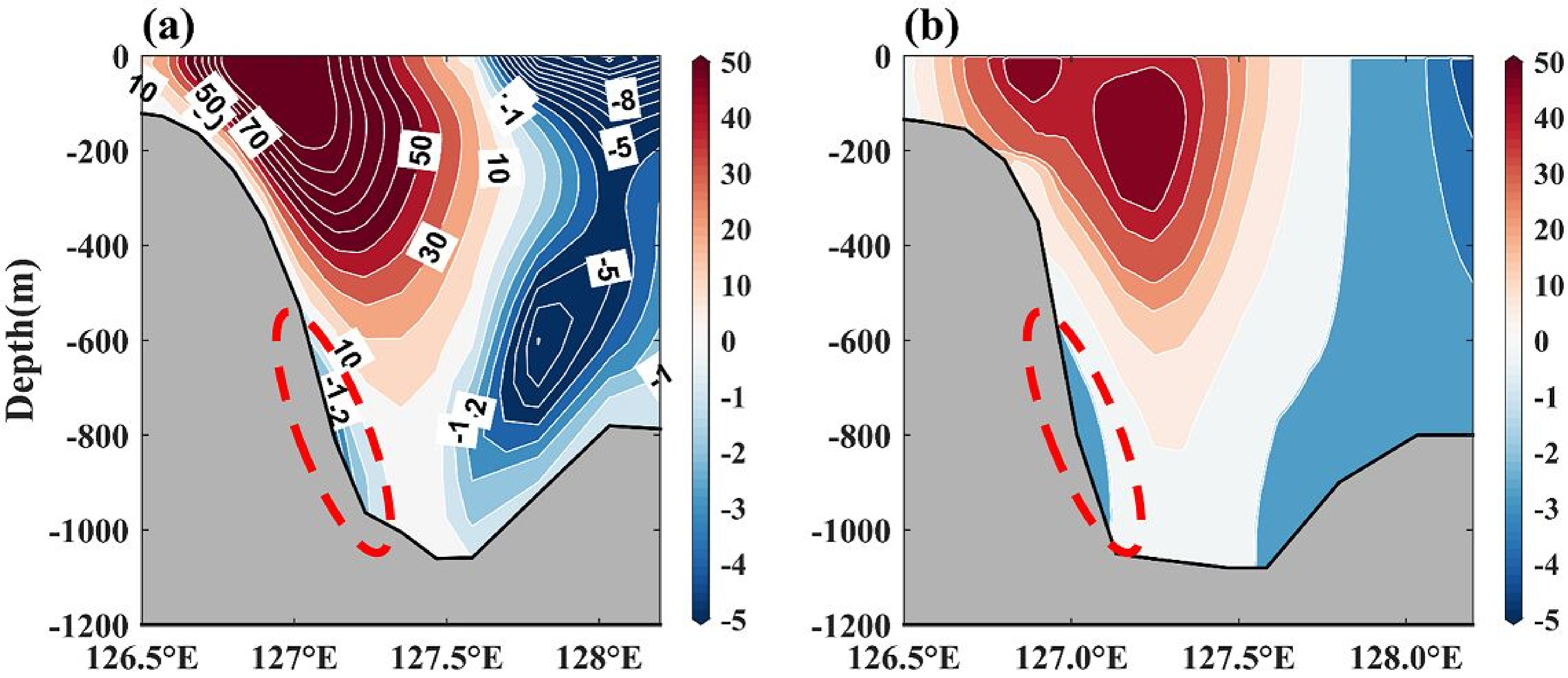
(a)
(b)
Depth(m)
0
-200
-400
-600
-800
-1000
-1200
126.5°E
127°E
127.5°E
128°E
127.0°E
128.0°E
50
40
30
20
10
0
-1
-2
-3
-4
-5
70
-8
-5
-1.2

Figure 3.

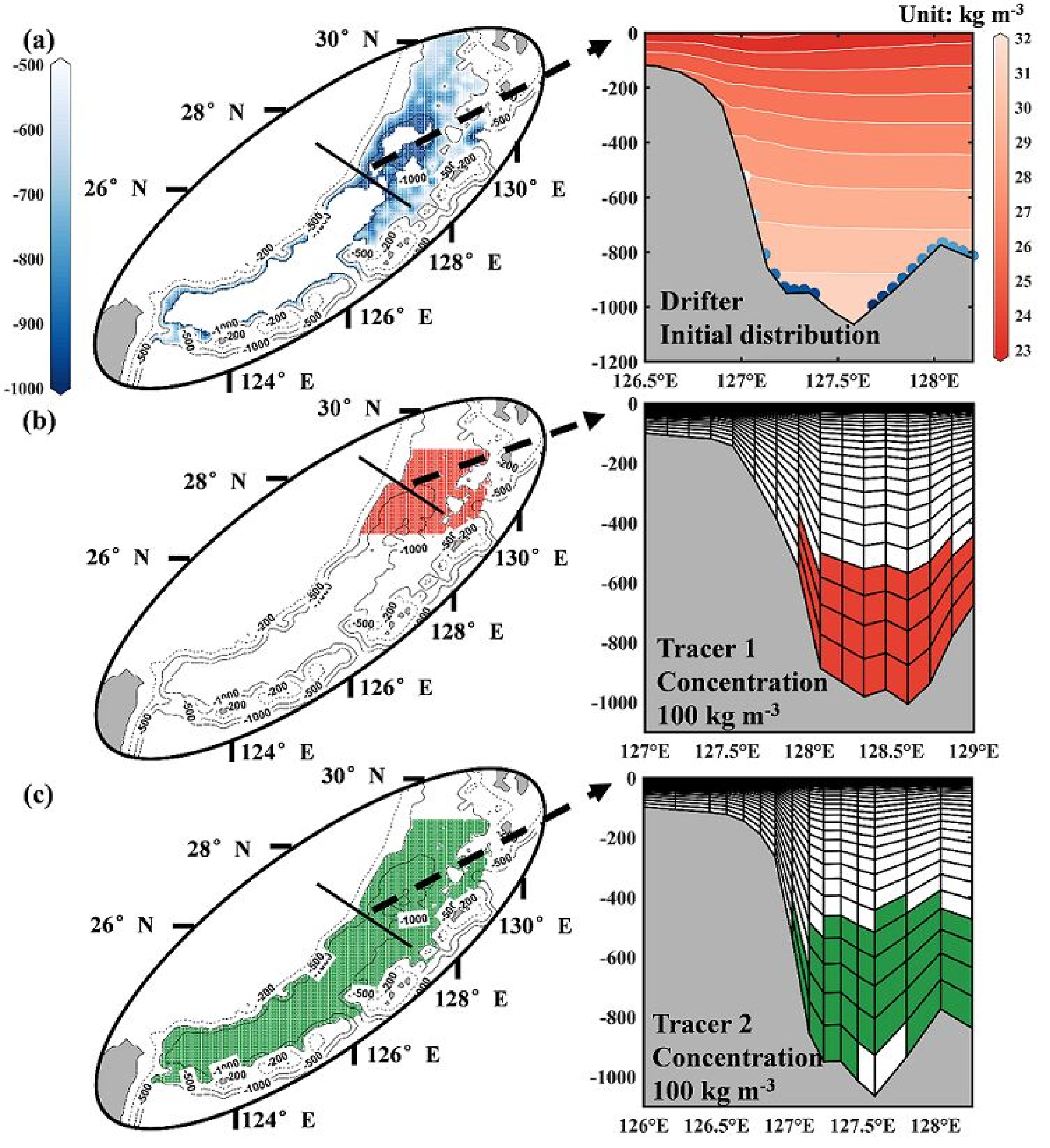

(a)
Unit: kg m-3
Drifter
Initial distribution
(b)
Tracer 1
Concentration
100 kg m-3
(c)
Tracer 2
Concentration
100 kg m-3

Figure 4.

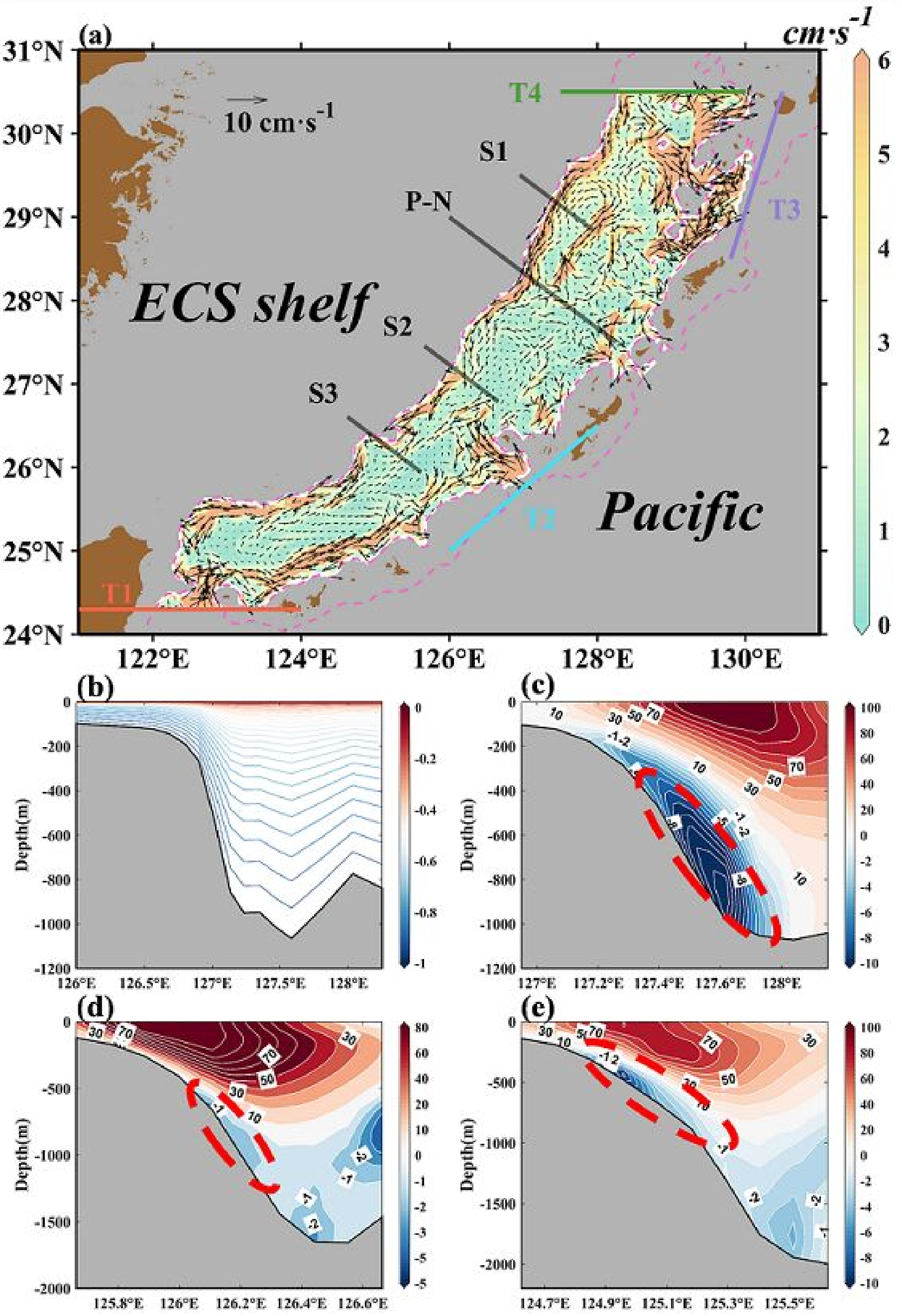

(a)
cm·s-1
T4
10 cm·s-1
S1
P-N
T3
ECS shelf
S2
S3
Pacific
T2
T1
31°N
30°N
29°N
28°N
27°N
26°N
25°N
24°N
122°E
124°E
126°E
128°E
130°E
(b)
(c)
(d)
(e)
Depth(m)

Figure 5.

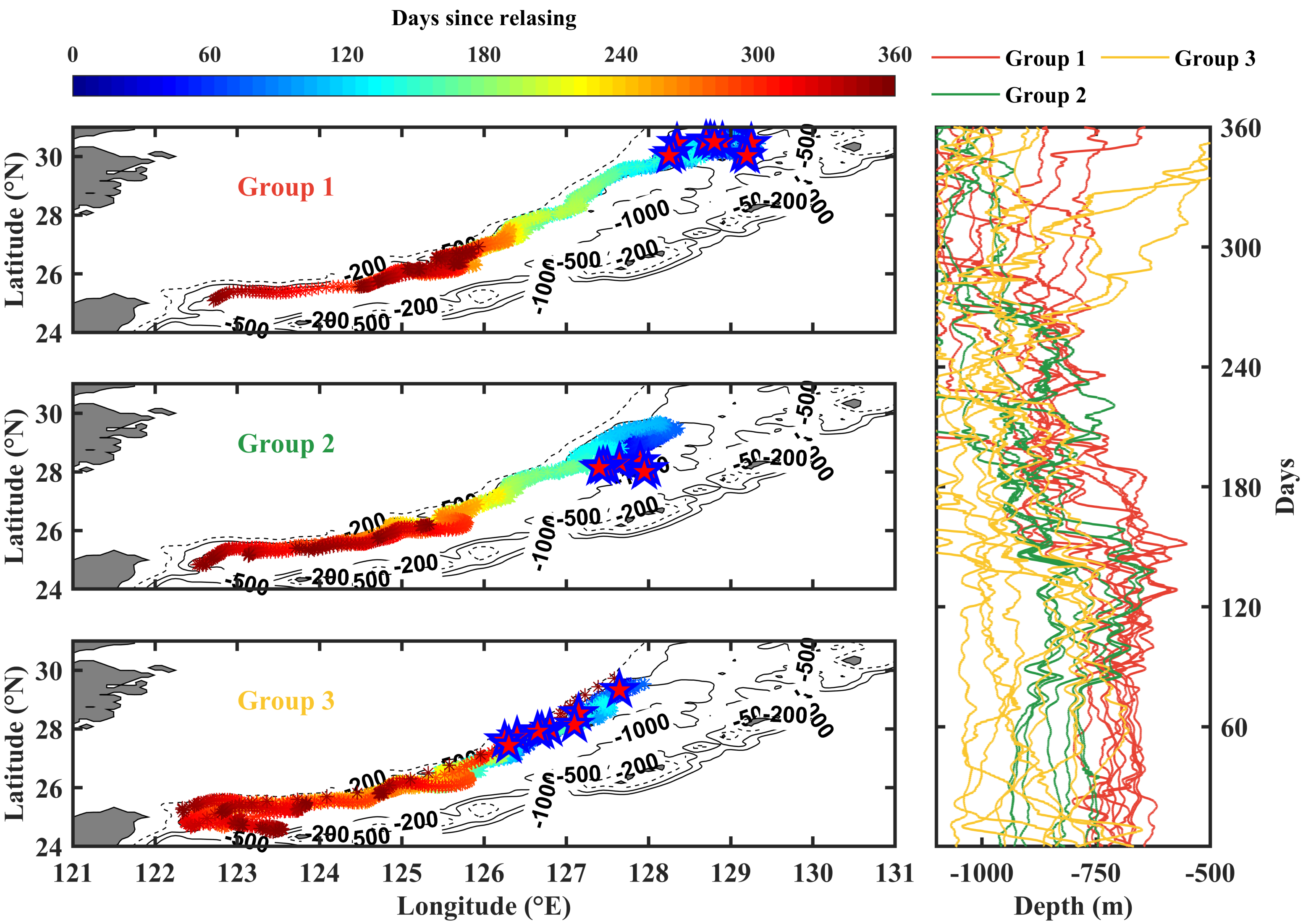

Days since relasing
0
60
120
180
240
300
360
Group 1
Group 2
Group 3
Latitude (°N)
Longitude (°E)
Depth (m)
Days

Figure 6.

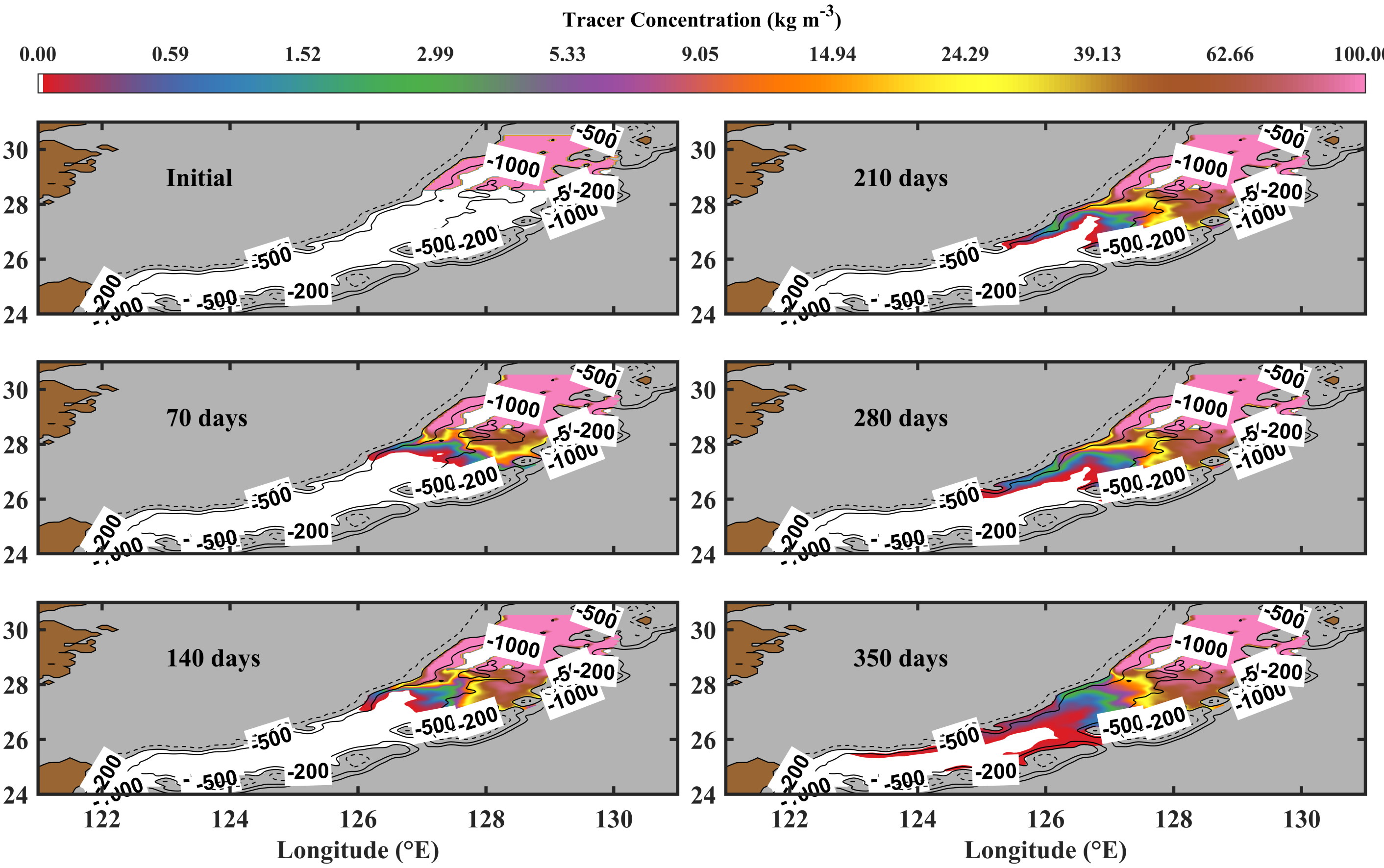

Tracer Concentration (kg m^{-3})
0.00
0.59
1.52
2.99
5.33
9.05
14.94
24.29
39.13
62.66
100.00
Initial
70 days
140 days
210 days
280 days
350 days
-500
-1000
-200
-1000
-500
-200
-500
-500
-200
30
28
26
24
122
124
126
128
130
Longitude (°E)

Figure 7.

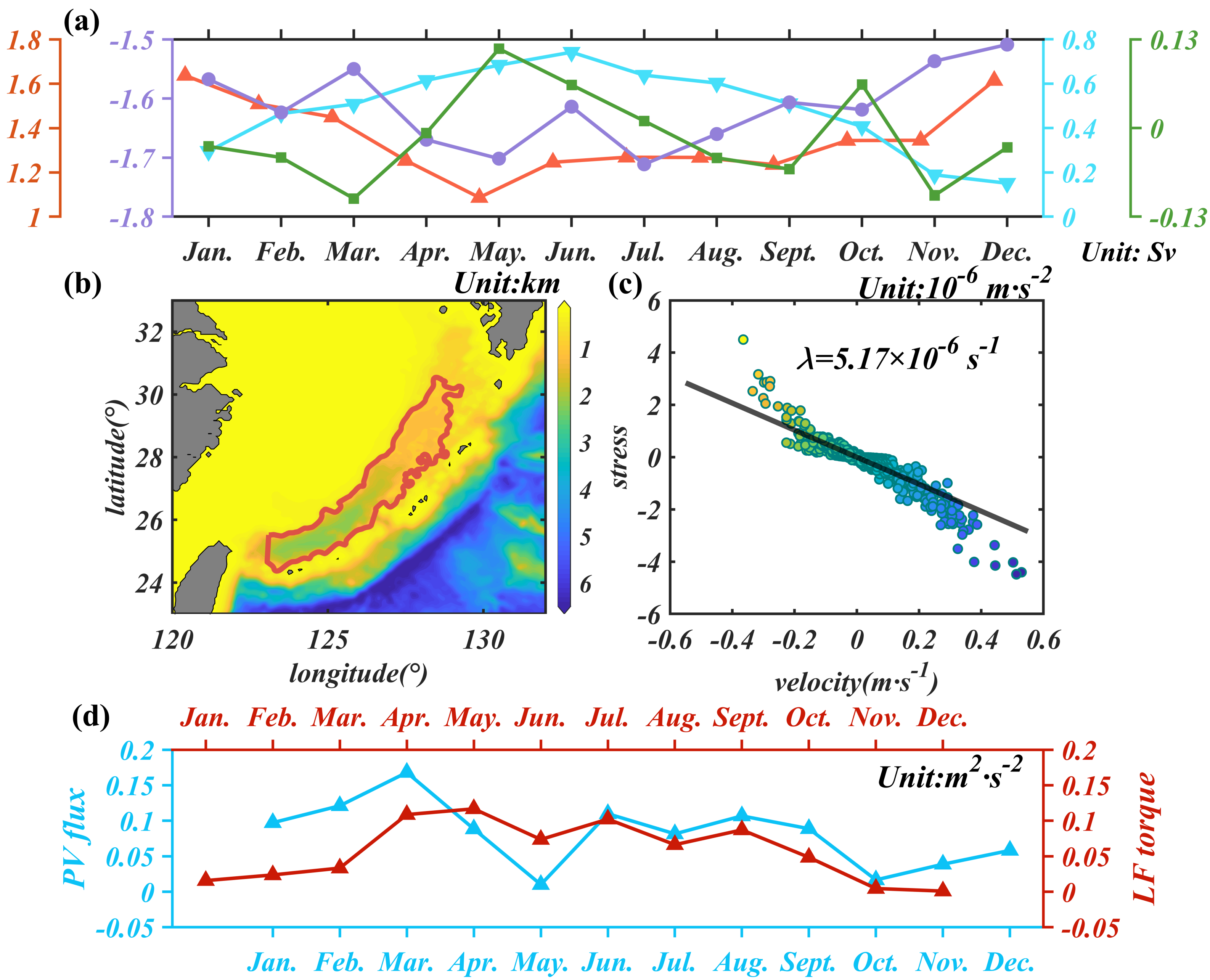
(a)
Unit: Sv
Jan. Feb. Mar. Apr. May. Jun. Jul. Aug. Sept. Oct. Nov. Dec.
(b)
Unit:km
latitude(°)
longitude(°)
(c)
Unit:10^-6 m·s^-2
λ=5.17×10^-6 s^-1
stress
velocity(m·s^-1)
(d)
Unit:m^2·s^-2
PV flux
LF torque

Figure 8.

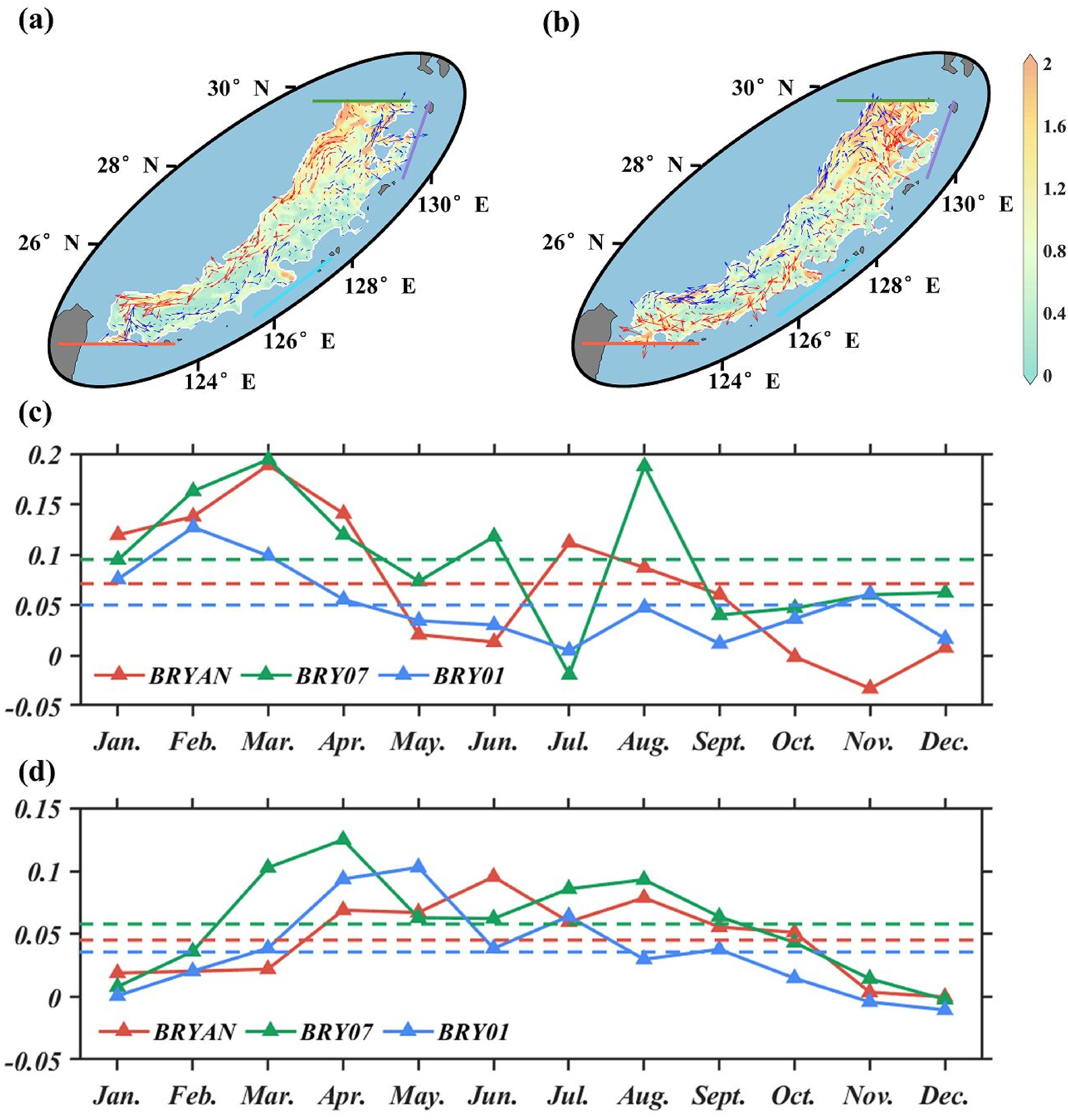

(a)
(b)
30° N
28° N
26° N
130° E
128° E
126° E
124° E
2
1.6
1.2
0.8
0.4
0
(c)
0.2
0.15
0.1
0.05
0
-0.05
BRYAN
BRY07
BRY01
Jan.
Feb.
Mar.
Apr.
May.
Jun.
Jul.
Aug.
Sept.
Oct.
Nov.
Dec.
(d)
0.15
0.1
0.05
0
-0.05
BRYAN
BRY07
BRY01
Jan.
Feb.
Mar.
Apr.
May.
Jun.
Jul.
Aug.
Sept.
Oct.
Nov.
Dec.

Figure 9.

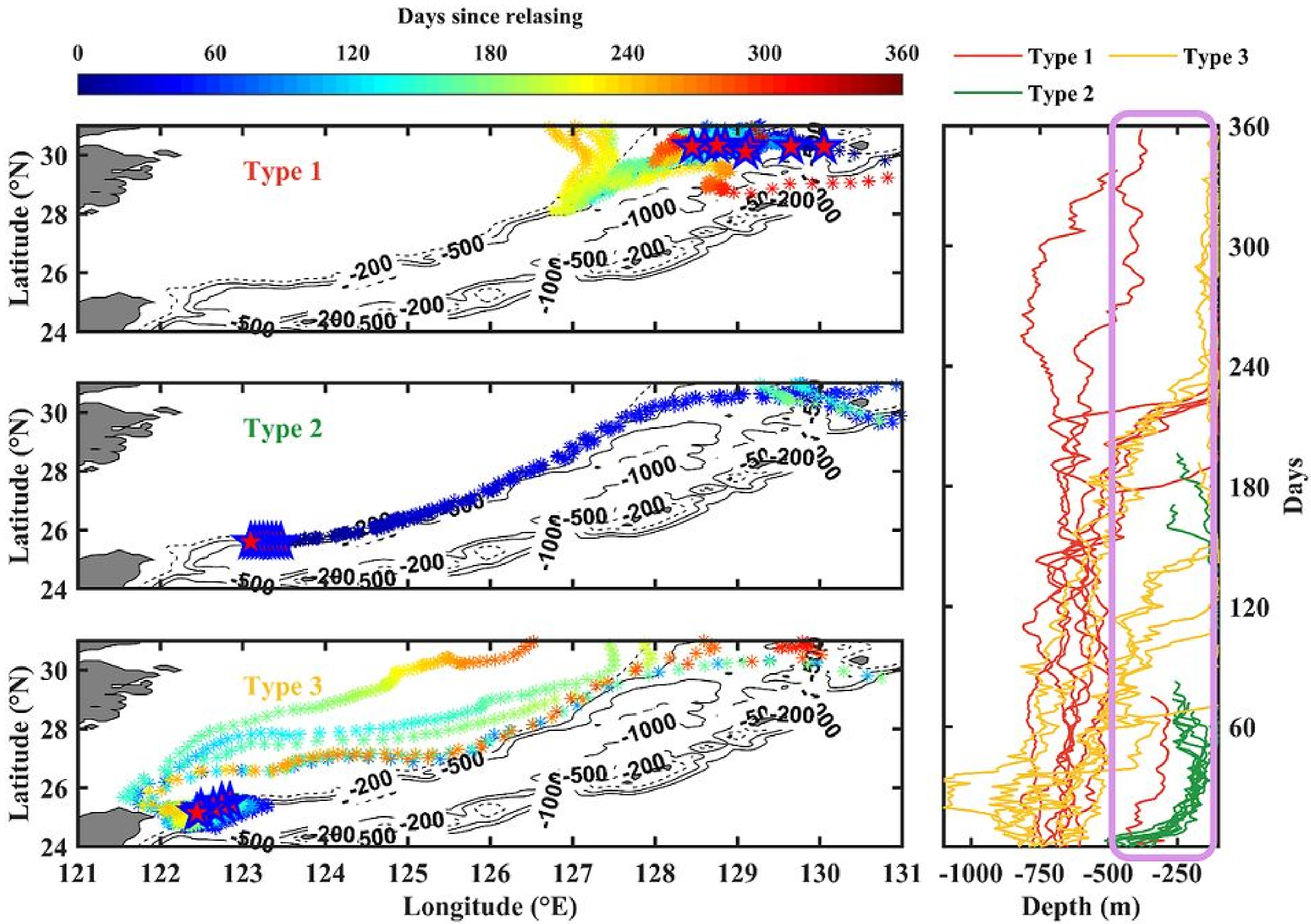
Days since relasing
0 60 120 180 240 300 360
Type 1
Type 2
Type 3
Latitude (°N)
Longitude (°E)
Depth (m)
Days
-1000
-500
-200
-50

Figure 10.

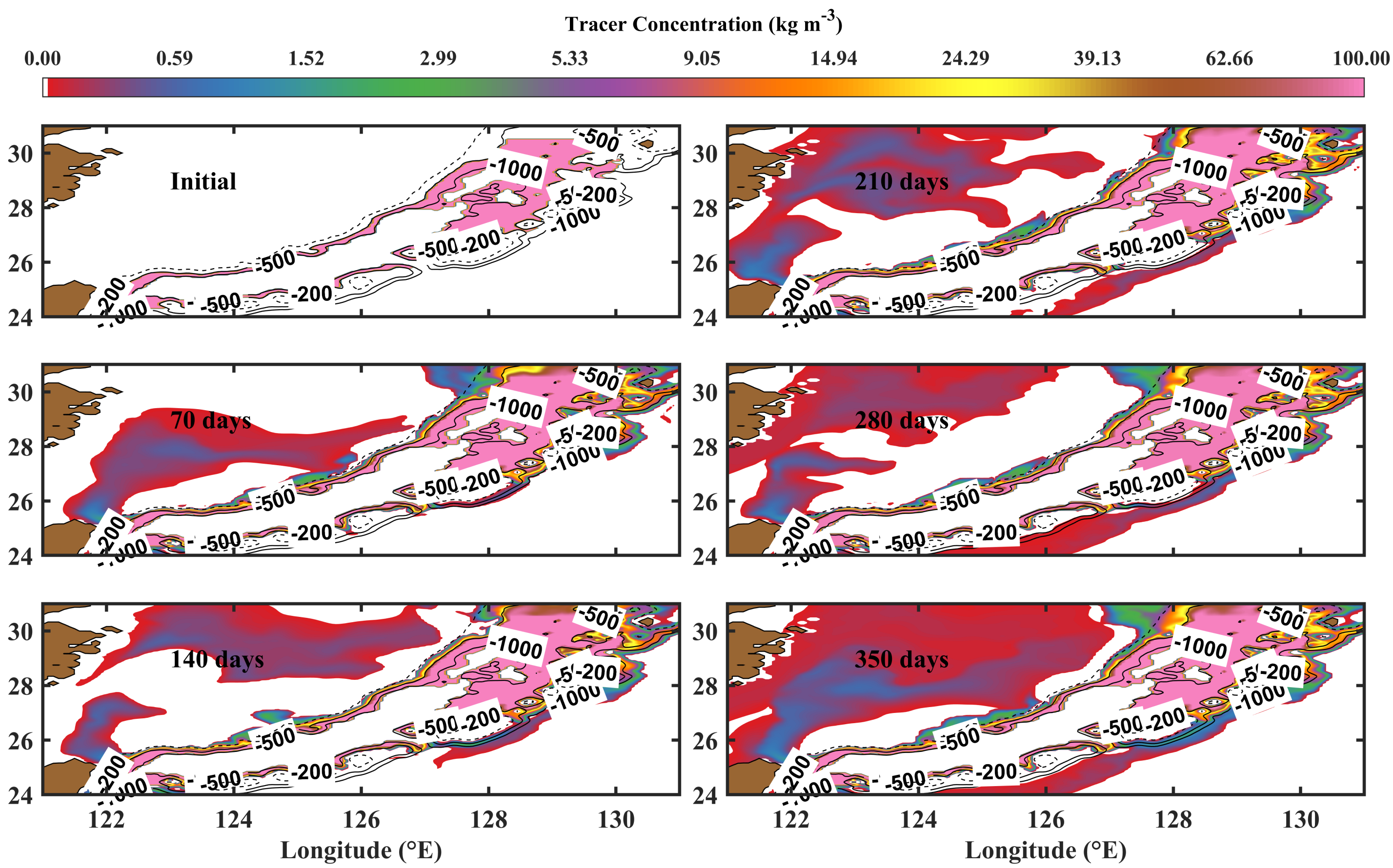

Tracer Concentration (kg m^{-3})
0.00
0.59
1.52
2.99
5.33
9.05
14.94
24.29
39.13
62.66
100.00
Initial
70 days
140 days
210 days
280 days
350 days
-500
-1000
-200
-500-200
Longitude (°E)

Figure 11.

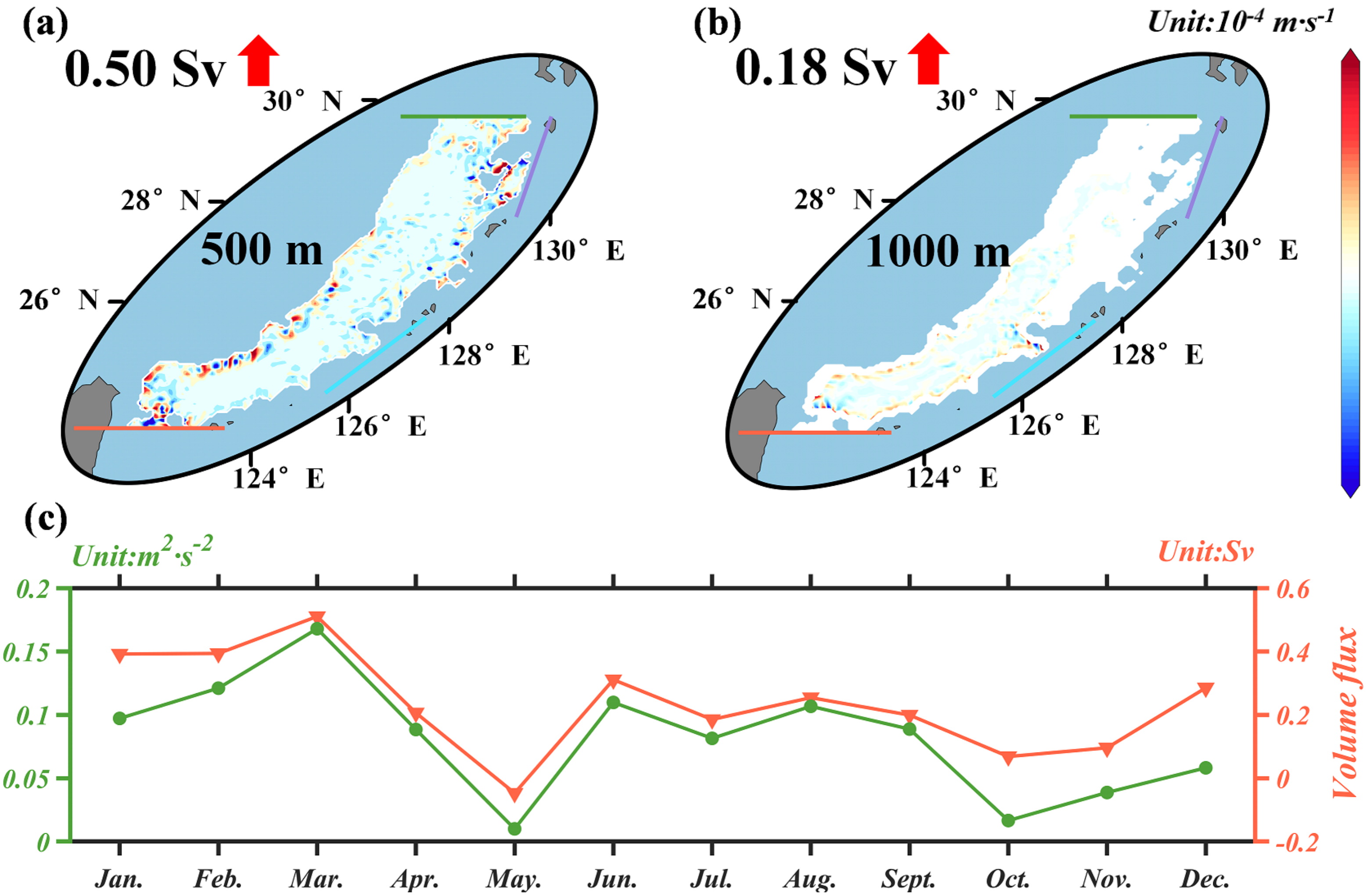
(a)
0.50 Sv
30° N
28° N
26° N
500 m
130° E
128° E
126° E
124° E
(b)
0.18 Sv
Unit:10-4 m·s-1
30° N
28° N
26° N
1000 m
130° E
128° E
126° E
124° E
5
3
1
-1
-3
-5
(c)
Unit:m2·s-2
Unit:Sv
PV flux
Volume flux
0.2
0.15
0.1
0.05
0
0.6
0.4
0.2
0
-0.2
Jan.
Feb.
Mar.
Apr.
May.
Jun.
Jul.
Aug.
Sept.
Oct.
Nov.
Dec.

Figure 12.

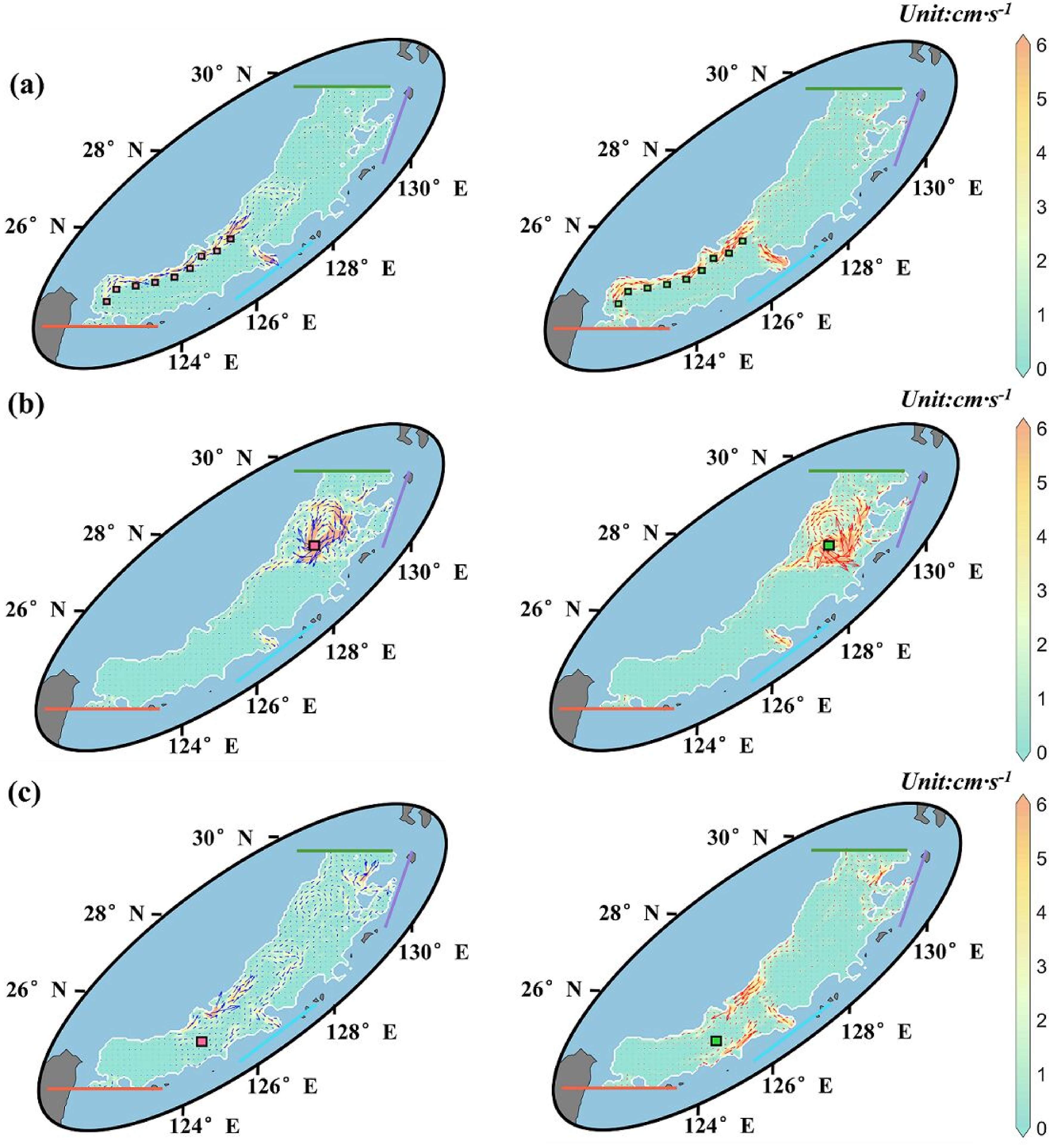
(a)
(b)
(c)
Unit:cm·s-1
30° N
28° N
26° N
130° E
128° E
126° E
124° E
0
1
2
3
4
5
6

Figure 13.

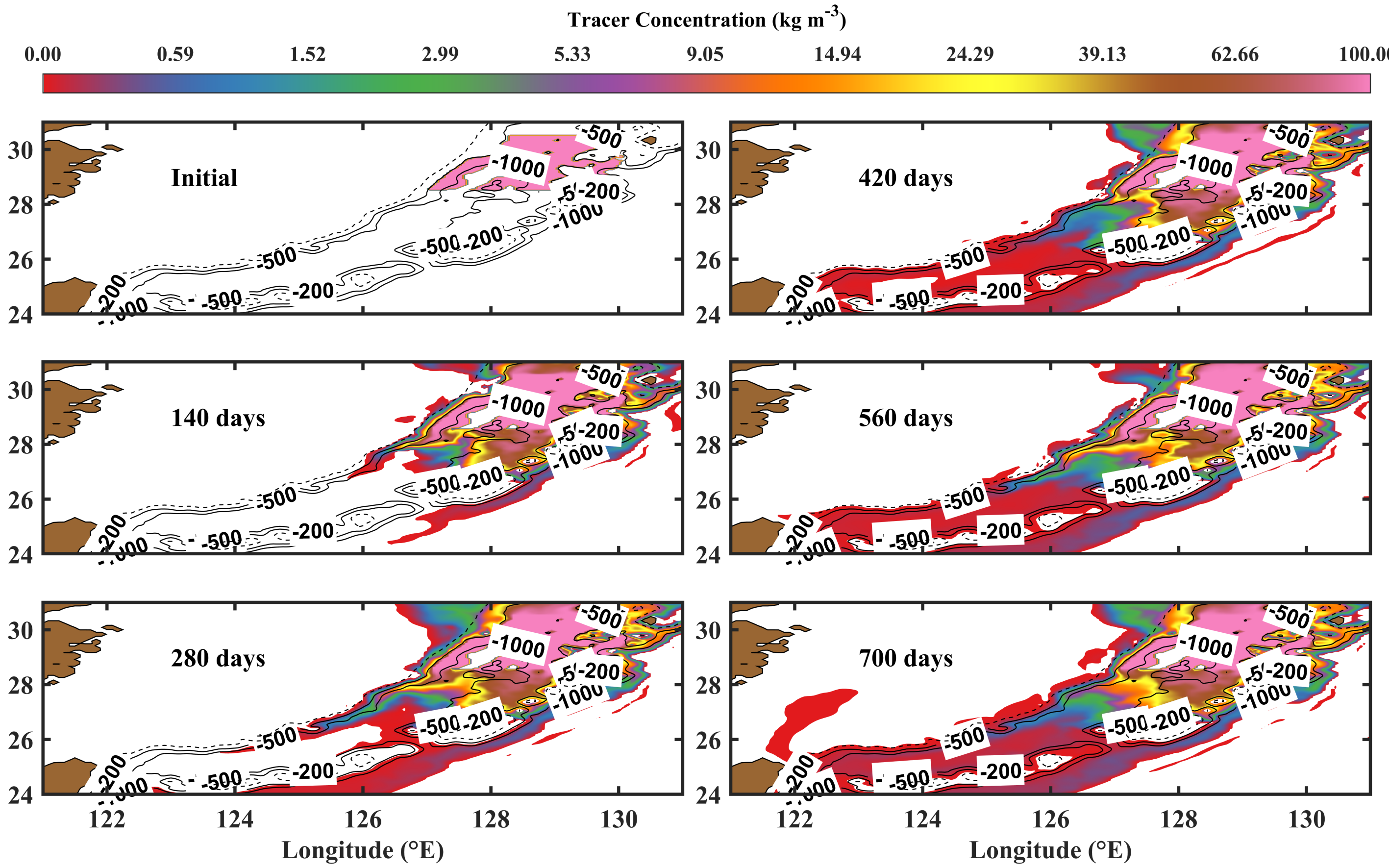

Tracer Concentration (kg m^{-3})
0.00
0.59
1.52
2.99
5.33
9.05
14.94
24.29
39.13
62.66
100.00
Initial
140 days
280 days
420 days
560 days
700 days
-500
-1000
-200
30
28
26
24
122
124
126
128
130
Longitude (°E)

Figure 14.

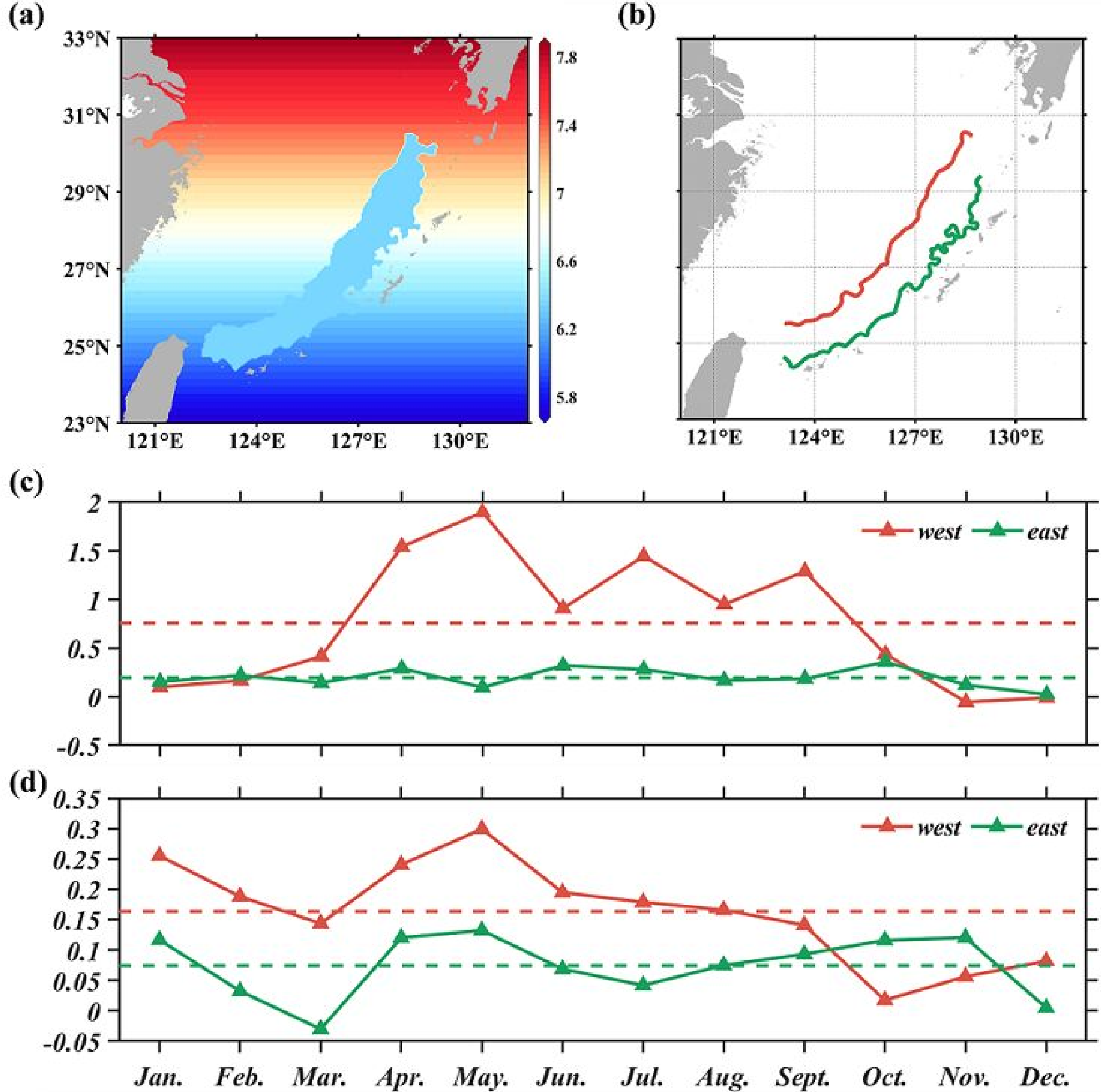
(a)
33°N
31°N
29°N
27°N
25°N
23°N
121°E
124°E
127°E
130°E
7.8
7.4
7
6.6
6.2
5.8
(b)
121°E
124°E
127°E
130°E
(c)
2
1.5
1
0.5
0
-0.5
west
east
(d)
0.35
0.3
0.25
0.2
0.15
0.1
0.05
0
-0.05
west
east
Jan.
Feb.
Mar.
Apr.
May.
Jun.
Jul.
Aug.
Sept.
Oct.
Nov.
Dec.

Figure 15.

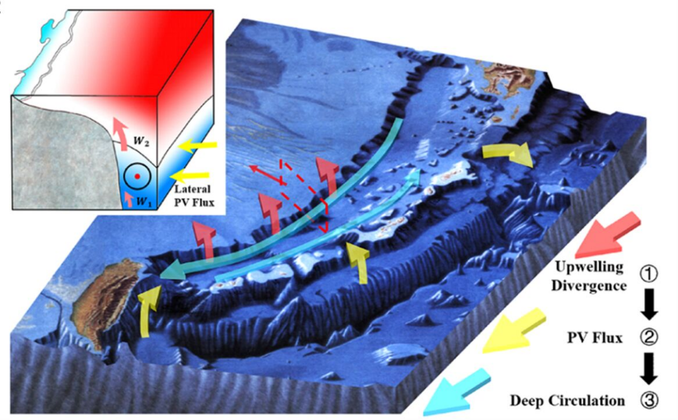

W_2
W_1
Lateral PV Flux
Upwelling Divergence ①
PV Flux ②
Deep Circulation ③